

# D-Band Channel Measurements and Characterization for Indoor Applications

Seunghwan Kim, *Student Member, IEEE*, Wasif Tanveer Khan, *Member, IEEE*,  
Alenka Zajić, *Senior Member, IEEE*, and John Papapolymou, *Fellow, IEEE*

**Abstract**—This paper presents measurements and characterization of D-band indoor channels. The measurements are performed in line-of-sight (LoS), obstructed-LoS (OLOs), and reflected non-LoS (RNLoS) environments. For OLoS scenario, cylindrical objects of different materials are used as an obstruction. For RNLoS, different surfaces are used as reflectors. From the large set of LoS and OLoS measured data, the parameters for single-slope path loss model with shadowing are devised. Furthermore, the analysis of multipath propagation is performed. The results show that strong multiple reflections from the transmitter and receiver electronics are present both in LoS and OLoS environments. Additionally, the results show that glass and ceramic objects in the propagation path produce surface-diffracted rays which clock-wise and counter clock-wise superposition leads to frequency-dependent path loss. Finally, the results show that the RNLoS measured path loss with aluminum plate as a reflector is very similar to free-space path loss when the angle of incidence and the angle of reflection are equal.

**Index Terms**—Channel measurements, channel modeling, D-band channels, indoor channels.

## I. INTRODUCTION

ULTRA-WIDEBAND wireless communication systems are expected to help satisfy the ever-growing need for smaller devices that can offer higher speed wireless communications anywhere and anytime. In the past years, it has become obvious that wireless data rates exceeding 10 Gb/s will be required in several years from now [1]. To achieve this goal, several frequency bands have been explored. For example, propagation characteristics of 60 GHz with an unregulated bandwidth of 7 GHz have been presented in [2]–[10] and references therein. Similarly, propagation characteristics of 300 GHz with an unregulated bandwidth of 47 GHz have been presented in [11]–[25] and references therein. While 60-GHz communications have limited bandwidth, 300 GHz communications are limited in range.

As an alternative, the 60 GHz of spectrum from 110 to 170 GHz (D-band) offers a promising approach to provide

sufficient *bandwidth and range* required for ultra-fast and ultra-wideband data transmissions [26]. This frequency band is ideally suited for short- and medium-range communications. This large bandwidth paired with higher speed wireless links has potential applications in precision positioning and velocity sensors [27], passive millimeter-wave cameras [28] and can open the door to a large number of novel applications such as ultra-high-speed pico-cell cellular links, wireless short-range communications, and on-body communication for health monitoring systems. Note that this frequency band is currently unregulated for wireless communications, and is typically used for atmospheric applications.

To enable wireless communications in D-band, it is imperative to understand propagation mechanisms that govern communication at these frequencies. While D-band has been extensively used for microwave atmospheric sounding (e.g., [29]), to the best of our knowledge, *no indoor D-band* channel characterization based on measurements has been reported in the open literature. Although channel characterization at 120 GHz for an indoor office scenario has been reported in [30], the work only presents ray-tracing simulation results without channel measurements. While atmospheric absorption is the main focus of microwave atmospheric sounding, this loss plays minor role in indoor propagation. Reflections, diffraction, and scattering are more prevalent propagation mechanisms in indoor D-band channels.

As the first step toward characterizing D-band channel, we have performed line-of-sight (LoS), obstructed-LoS (OLOs), and reflected non-LoS (RNLoS) measurements at 140 with 60 GHz of bandwidth between the transmitter ( $T_x$ ) and the receiver ( $R_x$ ). The contributions of this paper are as follows.

- 1) Devised parameters for the single-slope path loss model with shadowing for LoS and OLoS environments. The results show that the path loss exponent is around 1.9 for LoS environment and the variations due to shadowing are negligible. Furthermore, the results show that the path loss exponent for plastic cup OLoS path is the closest to the LoS path loss exponent and that glass and ceramic OLoS path loss exponents increase to 3. Additionally, we find that glass and ceramics objects in the propagation path cause multiple strong reflections leading to higher frequency-dependent path loss. Finally, we observe that the RNLoS path loss with aluminum plate as a reflector is very similar to free-space path loss when the angle of incidence and reflection are equal. This indicates that communication is possible in RNLoS scenarios.

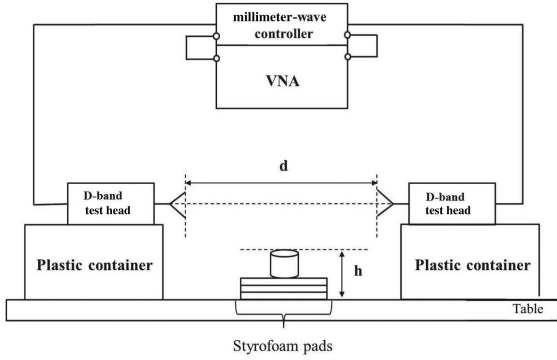
Manuscript received October 22, 2014; revised January 29, 2015; accepted April 02, 2015.

S. Kim, A. Zajić, and J. Papapolymou are with the School of Electrical and Computer Engineering, Georgia Institute of Technology, Atlanta, GA 30332 USA (e-mail: skim745@gatech.edu; alenka.zajic@ece.gatech.edu; john.papapolymou@ece.gatech.edu).

W. Khan is with the School of Electrical Engineering, Lahore University of Management Sciences (LUMS), Lahore 54792, Pakistan (e-mail: wasif.tanveer@lums.edu.pk).

Color versions of one or more of the figures in this paper are available online at <http://ieeexplore.ieee.org>.

Digital Object Identifier 10.1109/TAP.2015.2426831



F1:1 Fig. 1. 110–170 GHz measurement setup.

TABLE I  
MEASUREMENT PARAMETERST1:1  
T1:2

Parameter	Symbol	Value
Measurement points	N	801
Intermediate frequency bandwidth	$\Delta f_{IF}$	100 Hz
Average noise floor	$P_N$	-85 dBm
Input signal power	$P_{in}$	0 dBm
Start frequency	$f_{start}$	110 GHz
Stop frequency	$f_{stop}$	170 GHz
Bandwidth	B	60 GHz
Time domain resolution	$\Delta t$	0.0167 ns
Maximum excess delay	$\tau_m$	13 ns

- 88 2) Analyzed the rms delay spread  $\tau_{RMS}$ , the mean excess  
 89 delay  $\tau_m$ , and the coherence bandwidth for LoS, OLoS,  
 90 and RNLoS environments. In LoS environment, the mean  
 91 values of  $\tau_{RMS}$  and  $\tau_m$  are 12.84 and 16.95 ps, respec-  
 92 tively. The mean excess delay increases in the presence  
 93 of obstructions, with the smallest increase in the presence  
 94 of plastic cup and the largest increase in the presence of  
 95 ceramic mug. There is almost no increase in the mean  
 96 excess delay in RNLoS environment for aluminum plate  
 97 as a reflector and the equal angles of incidence and  
 98 reflection.
- 99 3) Analyzed the power delay profiles (PDPs) for LoS, OLoS,  
 100 and RNLoS environments. We can observe that the strong  
 101 reflections from the  $T_x$  and  $R_x$  electronics are present  
 102 both in LoS and OLoS environments. Additionally, OLoS  
 103 channels with obstructions of cylindrical shape, such  
 104 as a glass beaker, a plastic cup, or a ceramic mug,  
 105 also experience the diffraction at the convex surface of  
 106 the cylindrical obstruction. The creeping waves, or the  
 107 surface-diffracted rays that travel around the cylinder in  
 108 clock-wise and counter clock-wise directions superim-  
 109 pose leading to frequency dependant path loss.

110 The remainder of this paper is organized as follows.  
 111 Section II describes the measurement equipment, antennas used  
 112 in the measurements, and the measurement setup. Section III  
 113 presents the path loss, shadowing, and multipath propagation  
 114 analysis of LoS measured data. Section IV presents the path  
 115 loss, shadowing, and multipath propagation analysis of OLoS  
 116 measured data, while Section V presents the path loss and mul-  
 117 tipath propagation analysis of RNLoS measured data. Finally,  
 118 Section VI provides some concluding remarks.

## 119 II. MEASUREMENT SETUP

### 120 A. Equipment

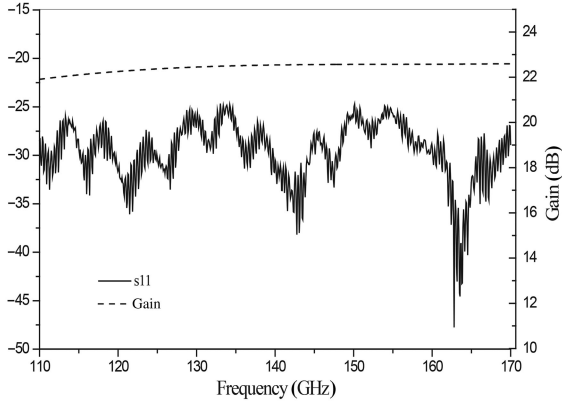
121 The block diagram of the D-band measurement setup is  
 122 shown in Fig. 1. The Agilent E8361C vector network analyzer  
 123 is used for all measurements. The E8361C has a frequency  
 124 range up to 67 GHz; therefore, the N5260A (millimeter-  
 125 wave controller) and OML V06VNA2 (millimeter-wave test  
 126 head modules) are used to extend the range to the D-band

(110–170 GHz). The N5260A millimeter-wave controller  
 127 provides radio frequency (RF) and local oscillator (LO) sig-  
 128 nals to the millimeter-wave test head modules and returns the  
 129 down-converted reference and test IF signals to the VNA for  
 130 process and display. The OML V06VNA2 frequency exten-  
 131 sion module has an LO multiplication factor of 10, which  
 132 up-converts the input LO frequency from 11 to 17 GHz,  
 133 supplied by the millimeter-wave controller, to the D-band  
 134 (110–170 GHz).  
 135

136 The full available bandwidth of 60 GHz is used in all mea-  
 137 surements, which provides the spatial and temporal resolution  
 138 of 5 mm or 0.0167 ns. Due to input power restrictions of the  
 139 mixers, a test signal with a power of 0 dBm is used, provid-  
 140 ing a dynamic range of approximately 90 dB for the chosen  
 141 intermediate frequency filter bandwidth of  $\Delta f_{IF} = 100$  Hz. The  
 142 number of sweep points is set to 801, and the maximum excess  
 143 delay is 13 ns. All measurement parameters are summarized in  
 144 Table I.

### 145 B. Antenna Characteristics

146 The antenna used in the measurement is a pyramidal horn  
 147 with gain that varies from 22 to 23 dBi from 110 to 170 GHz,  
 148 respectively. Both  $T_x$  and  $R_x$  antennas are vertically polar-  
 149 ized and have theoretical half-power beamwidth (HPBW) of  
 150  $12^\circ$  and  $13.5^\circ$  in E- and H-plane, respectively, at 110 GHz.  
 151 The E- and H-plane beamwidths also decrease to  $9^\circ$  and  $12^\circ$ ,  
 152 respectively, toward higher frequencies. Furthermore, antennas  
 153 have sidelobes that are at least 25 dB below the main beam  
 154 and all possible reflectors on the sides of the channel have been  
 155 covered with absorbers as shown in Fig. 3, to ensure that any  
 156 paths resulting from the sidelobes are suppressed. The mea-  
 157 sured  $S_{11}$  and the frequency-dependent gain of the horn antenna  
 158 are presented in Fig. 2. Note that the return loss shown here  
 159 includes the reflections at the interfaces between cable and test  
 160 head, as well as test head and the antenna due to mismatches  
 161 between them. Nevertheless, we can observe that the  $S_{11}$  is  
 162 below  $-25$  dB across the entire bandwidth. In further analy-  
 163 sis, antennas are considered to be part of the channel impulse  
 164 response, which is typically the case in wireless communication  
 165 applications.



F2:1 Fig. 2. Reflection coefficient and gain of the horn antenna used in measure-  
F2:2 ments.

### 166 C. Measurement Scenarios

167 In this measurement campaign, three different scenarios  
168 have been considered: LoS scenario shown in Fig. 3(a), OLoS  
169 scenario shown in Fig. 3(b), and RNLoS scenario shown in  
170 Fig. 3(c).

171 Considering the short-range of D-band applications, the  
172  $T_x$ – $R_x$  separation distance  $d$  shown in Fig. 1, has been varied  
173 from 35.56 (14") to 86.36 cm (34") in 5.08 cm (2") incre-  
174 ments, giving a total of 11 different distances for LoS scenario.  
175 Furthermore, to mitigate the reflections from the ground and the  
176 metallic transceiver cases, the  $T_x$  and  $R_x$  test heads have been  
177 placed on top of a supporting plastic container, and all possible  
178 reflecting surfaces, including the ground, the equipment rack  
179 cabinet, and the front faces of the test heads, have been cover-  
180 ed with absorbers as shown in Fig. 3(a). For OLoS scenario,  
181 obstructions of circular cylinder shape, i.e., cups, have been  
182 used as typical objects present on desk tops. To study the impact  
183 of different materials on propagation in D-band, three different  
184 types of material, i.e., glass, plastic (polystyrene), and ceramic  
185 have been considered. The same 11  $T_x$ – $R_x$  separations as in  
186 LoS scenario have been used for OLoS scenario. Each obstruc-  
187 tion is placed such that the cylinder's center coincides with the  
188 midpoint of the separation distance, and its top edge is 3.5 cm  
189 above the LoS path. Furthermore, to investigate the effect of  
190 obstruction height on path loss, we have varied the positions of  
191 the top rim of the cylinders, or  $h$  in Fig. 1, from 14.3 to 21.9 cm.  
192 The obstruction height has been varied by having different num-  
193 ber of styrofoam pads (which have been tested to cause minimal  
194 reflections at the frequencies of interest) underneath the cylin-  
195 der obstruction, as shown in Fig. 1. Note that the centers of the  
196 horn antennas are located 20.6 cm above the table. Finally, in  
197 RNLoS scenario, we use reflection as the main mechanism of  
198 wave propagation. Two types of reflecting surfaces, aluminum  
199 plate and fiberboard, having different reflectivity and surface  
200 roughness, have been used. Furthermore, by varying the angu-  
201 lar position of the  $R_x$ , while keeping the  $T_x$  position fixed,  
202 the range of  $R_x$  angular offsets at which the  $R_x$  can detect  
203 the reflected signal is studied. For RNLoS, the LoS separation  
204 distance was fixed to 76.2 cm.

## III. CHARACTERIZATION OF D-BAND LOS CHANNEL 205

### A. LoS Path Loss and Shadowing 206

In this paper, we refer to mean path loss as the transmit power  
multiplied by the transmit and receive antenna gains divided by  
the mean received power, i.e.,

$$PL = \frac{P_t \cdot G_t \cdot G_r}{\bar{P}_r} = \left( \frac{4\pi d}{\lambda} \right)^2. \quad (1)$$

The mean path loss is obtained by averaging a swept contin-  
uous wave over time and frequency, i.e.,

$$PL(d) = \frac{1}{MN} \sum_{i=1}^N \sum_{j=1}^M |H(f_i, t_j, d)|^2 \quad (2)$$

where  $H(f_i, t_j, d)$  is the measured complex frequency response  
data matrix,  $N$  is the number of observed frequencies,  $M$  is the  
number of frequency-response snapshots over time, and  $d$  is the  
distance in meters.

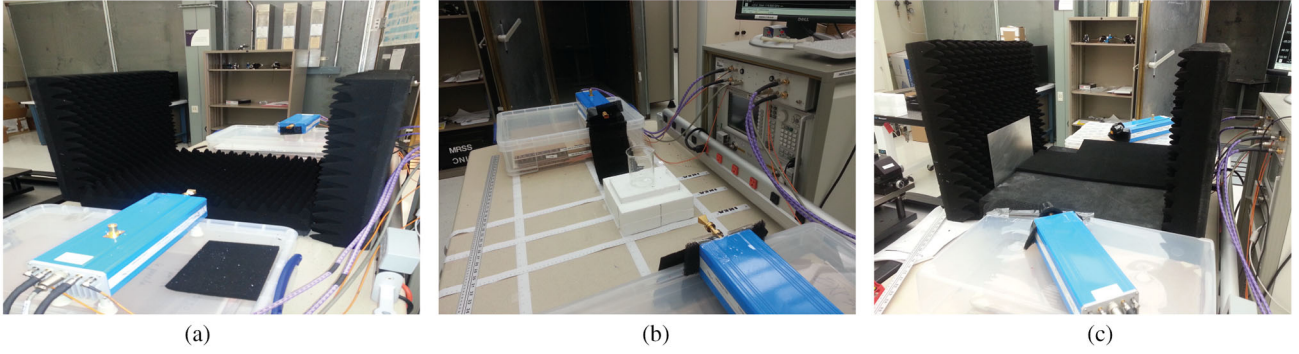
Fig. 4 compares the measured path loss with the theoretical  
path loss calculated using (1). We plot only 5 out of 11 separa-  
tion distances to avoid clutter. We can observe that the measured  
path loss curves very closely follow the theoretical lines. The  
oscillations observed in the path loss curves have been found  
to be a result of multiple reflections between the front faces of  
the  $T_x$  and  $R_x$  test heads. Although they were covered  
with a layer of absorbing material, as shown in Fig. 3(a), it  
was apparently not thick enough to completely mitigate the  
reflections. This resulted in the constructive and destructive  
interference between the direct and reflected rays, which led  
to the oscillation in the measured  $S_{21}$ .

Fig. 5 shows the scatter plot of the mean path loss as a func-  
tion of transmitter–receiver (T–R) separation on a desktop for  
an LoS environment. We can observe that the variation between  
different frequency-response snapshots over time is minimal.  
This is because there are no temporal or spatial variations nor  
additional clutter in the channel that would cause significant  
variations in the measured path loss. Note that this finding is  
significantly different from typical indoor measurements, where  
path loss significantly varies around the mean value. This find-  
ing leads us to conclude that the number of frequency-response  
snapshots over time does not have to be large and we have found  
that ten measurements are sufficient to capture all temporal  
variations in the signal.

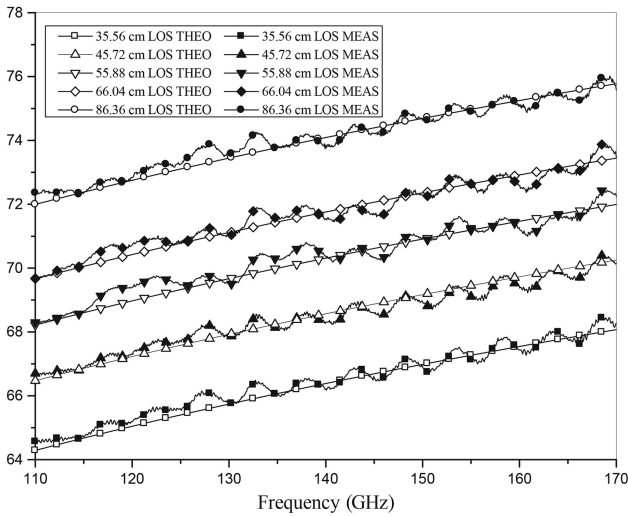
Path loss over distance can be modeled by the path loss  
exponent model [31], i.e.,

$$PL(d) = 10\gamma \log_{10} \left( \frac{d}{d_0} \right) + PL(d_0) + X_\sigma \quad (3)$$

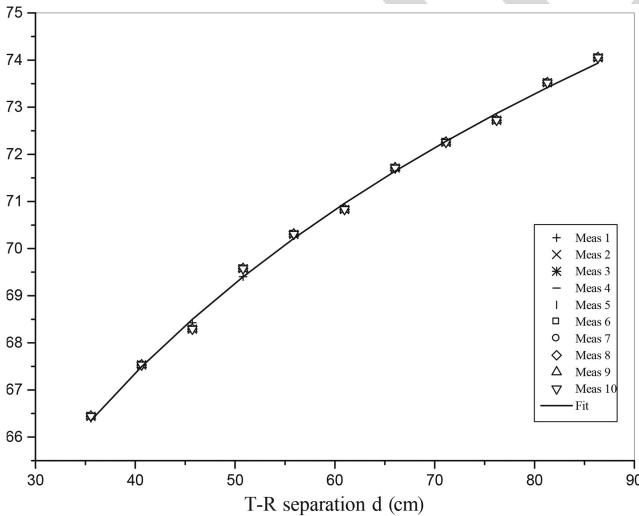
where  $PL(d)$  is the average path loss in dB at the distance  $d$ ,  
 $PL(d_0)$  is the free-space path loss at the reference distance  $d_0$ ,  
 $\gamma$  is the path loss exponent that characterizes how fast the path  
loss increases with the increase in the separation between the  
 $T_x$  and the  $R_x$ , and  $X_\sigma$  represents shadow fading that can be  
modeled as a zero-mean Gaussian distributed random variable  
(in dB) with standard deviation  $\sigma$ . Single slope path loss model



F3:1 Fig. 3. Photographs of measurement scenarios. (a) LoS. (b) OLoS, glass as obstruction. (c) RNLoS, aluminum plate as reflector.

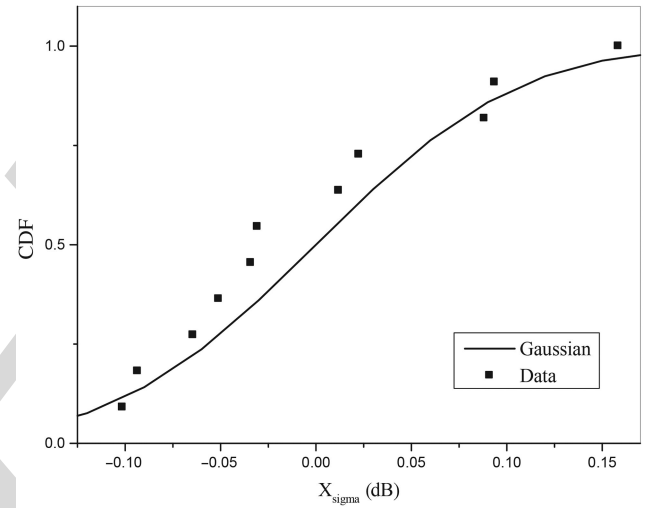


F4:1 Fig. 4. Measured and theoretical path loss for five separation distances.



F5:1 Fig. 5. Scatter plot of the LoS path loss.

250 is a statistical method used to estimate the path-loss slope and  
 251 the variation from the mean path loss. This is an important tool  
 252 when designing communication systems. More advanced statisti-  
 253 cal models can be devised from the measurements if the



F6:1 Fig. 6. Confirming the log-normality of the shadow fading caused by variations  
 F6:2 in T-R alignment in LoS environment.

single slope model does not produce adequate fit, which is not  
 254 the case in our paper. Alternative approach is a deterministic  
 255 approach (e.g., ray-tracing [22] and diffraction modeling [23]),  
 256 which is expected to produce more repeatable results; however,  
 257 it depends on the detailed and accurate description of all objects  
 258 in the propagation space.  
 259

To estimate the path loss model parameters  $\gamma$  and  $\sigma$ (dB)  
 260 in (3), we have performed the least-squares linear regression  
 261 fitting through the scatter of measured path loss points in deci-  
 262 bels such that the root mean square (rms) deviation of path  
 263 loss points about the regression line is minimized. The refer-  
 264 ence distance is  $d_0 = 1$  m and the free-space path loss at the  
 265 reference distance  $d_0$  is  $PL(d_0) = 75.19$  dB. The found path  
 266 loss exponent is around 1.97 and the variations due to shad-  
 267 owing are around  $\sigma = 0.12$  dB. To confirm that shadowing  
 268 can be modeled as a zero-mean Gaussian distributed random  
 269 variable, Fig. 6 compares the measured distribution of shadow  
 270 fading with the Gaussian distribution. This shadowing is due  
 271 to misalignment between the  $T_x$  and  $R_x$  antennas. While this  
 272 may not be a conventional shadowing process, it is still a ran-  
 273 dom process that causes variations of received power at a given  
 274 distance.  
 275

T2:1  
T2:2  
T2:3

TABLE II  
MEAN EXCESS DELAY, RMS DELAY SPREAD, AND COHERENCE  
BANDWIDTH FOR DIFFERENT T-R SEPARATION DISTANCES

d (cm)	Without absorbers			With absorbers		
	$\tau_m$ (ps)	$\tau_{rms}$ (ps)	$B_c$ (GHz)	$\tau_m$ (ps)	$\tau_{rms}$ (ps)	$B_c$ (GHz)
35.56	17.18	32.12	4.95	16.92	12.00	13.26
55.88	17.08	30.50	5.22	16.95	12.84	12.40
76.2	17.04	31.28	5.09	16.87	10.03	15.87

### 276 B. LoS Multipath Characterization

277 Multipath propagation is the propagation mechanism mani-  
278 fested when the transmitted signal reaches the receive antenna  
279 along two or more paths. Such waves typically arrive at the  $R_x$   
280 from many different directions and with different delays, and  
281 combine vectorially at the  $R_x$  antenna. Such channel impulse  
282 response can be characterized as [31]

$$h(t, \tau, d) = \sum_{k=1}^L a_k(t, d) \exp(j\theta_k(t, d)) \delta(t - \tau_k) \quad (4)$$

283 where  $L$  is the number of multipath components,  $a_k$  represents  
284 the amplitude of the  $k$ th multipath component,  $\theta_k$  is the associ-  
285 ated phase, and  $\tau_k$  is the excess delay of the  $k$ th path relative to  
286 the first arrival, and  $\delta(\cdot)$  denotes the Dirac delta function.

287 An estimate of the channel impulse response is made by  
288 taking the inverse discrete Fourier transform (IDFT) of the  
289 measured frequency response. The impulse response is then  
290 normalized such that the area under the squared magnitude  
291 of the power-delay response is equal to one. We refer to a  
292 normalized squared magnitude of the impulse response as the  
293 multipath intensity profile (MIP) at the single point in space.  
294 The noise floor of the MIP is set to 10 dB above the average  
295  $R_x$  noise floor. Part of the MIP characterization is based on  
296 rms delay spread  $\tau_{rms}$ , which is a measure of multipath spread  
297 within the channel. It is an important parameter for characteriz-  
298 ing time dispersion or frequency selectivity. It is the square root  
299 of the second central moment of the MIP and is given by [31]

$$\tau_{rms} = \sqrt{\sum_{k=1}^L (\tau_k - \tau_m)^2 |h(t, \tau_k, d)|^2} \quad (5)$$

300 where  $\tau_m$  is the mean excess delay (the first moment of the  
301 MIP) and is defined as

$$\tau_m = \sum_{k=1}^L \tau_k \cdot |h(t, \tau_k, d)|^2. \quad (6)$$

302 The rms delay spread, mean excess delay, and the coher-  
303 ence bandwidth ( $B_c = 1/(2 \cdot \pi \cdot \tau_{rms})$ ) for three separation  
304 distances with and without the absorbers are presented in  
305 Table II. It is observed that the coherence bandwidths have  
306 almost doubled, or even tripled, when the absorbers are in  
307 place.

308 For the distance of 35.56 cm, the delay spread  $\tau_{rms}$  is  
309 expected to be lower, or equivalently, the coherence bandwidth  
310 is expected to be higher than that of the 76.20 cm, but the

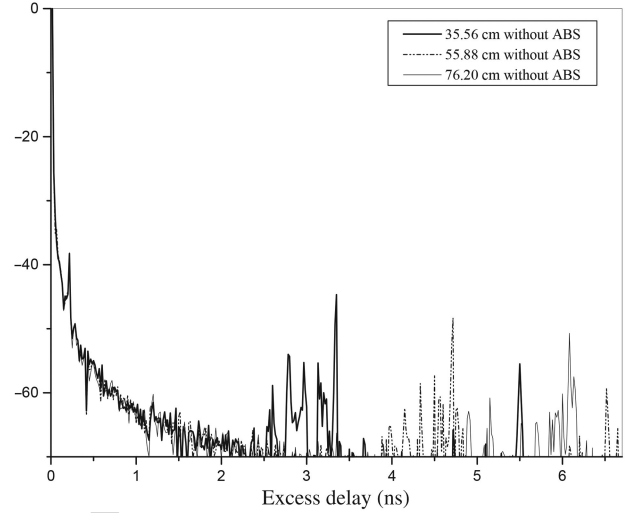


Fig. 7. Normalized PDPs for the three separation distances *without* absorbers. F7:1

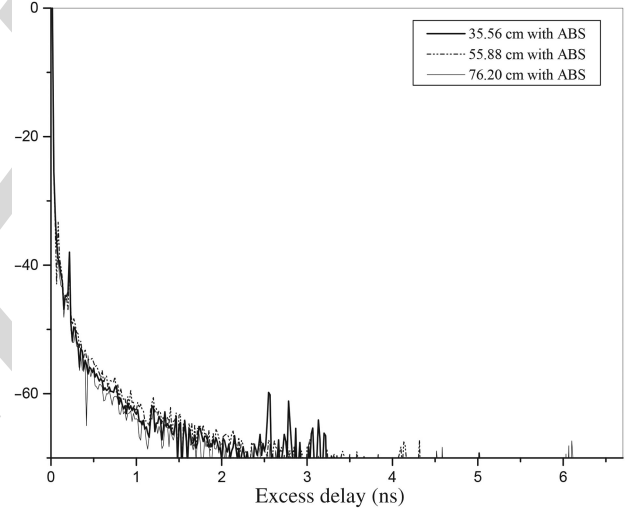
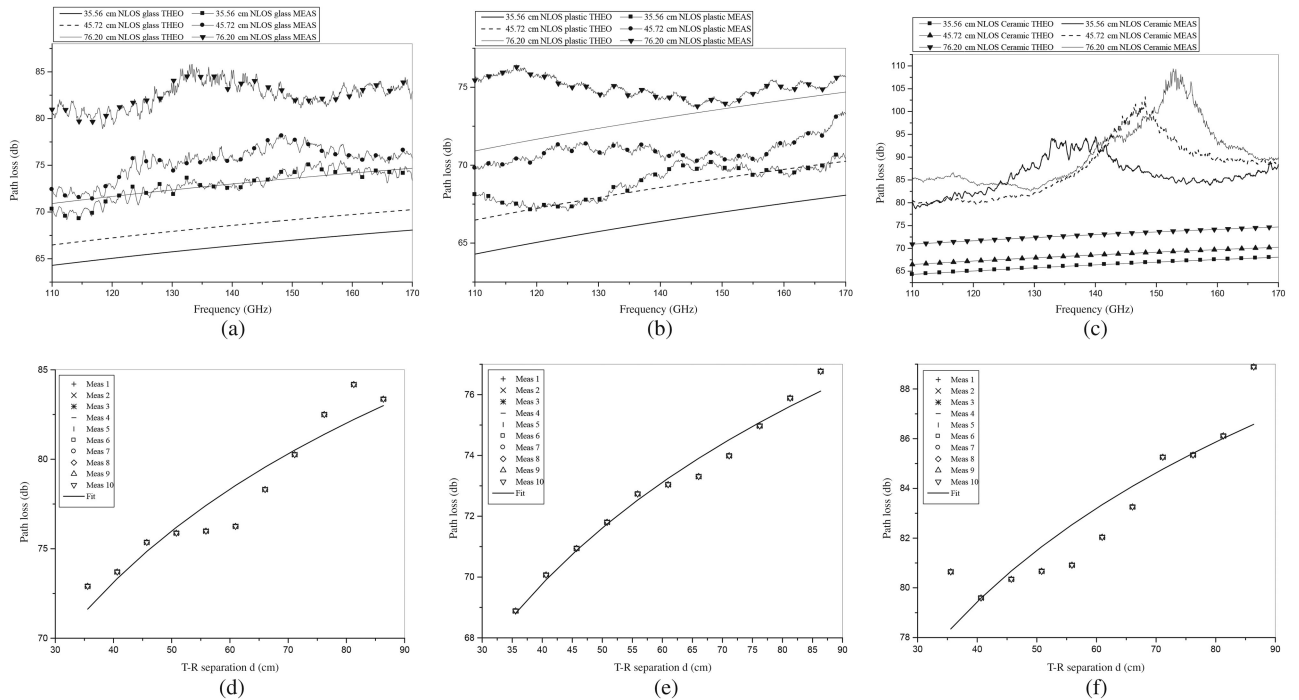


Fig. 8. Normalized PDPs for the three separation distances *with* absorbers. F8:1

opposite is observed in Table II. This is because the distance 311  
of 35.56 cm is short enough for the second reflected path to 312  
be captured within the maximum excess delay of 6.67 ns. This 313  
detection of an extra reflected signal results in the increase in 314  
the delay spread, which leads to the decrease in the coherence 315  
bandwidth. When the absorbers are used to cover the  $T_x/R_x$  test 316  
head's front face, we can observe that, while the reflections are 317  
almost completely removed for 76.20 cm, there are still some 318  
weak reflections observed for 35.56 cm. This has again resulted 319  
in a slightly narrower coherence bandwidth for 35.56 cm than 320  
that for 76.20 cm. 321

The PDP of the three separation distances in LoS environ- 322  
ment with and without the absorbers that cover the  $T_x$  and  $R_x$  323  
test heads is shown in Figs. 7 and 8. Note that all PDP's are 324  
normalized, and referenced to the first incoming path. We can 325  
observe that the later arriving paths caused by reflections off the 326  
metallic test head cases can be attenuated using the absorbers. It 327  
is also observed that the reflected paths have increasing excess 328  
delay, more delay spread, and decreasing signal power with 329



F9:1 Fig. 9. Path loss in OLoS scenario as a function of frequency, where the obstructions are (a) glass beaker; (b) plastic cup; and (c) ceramic mug (upper row) and  
 F9:2 the path loss scatter plot as a function of distance (lower row) for OLoS scenarios, where the obstructions are (d) glass beaker; (e) plastic cup; and (f) ceramic mug.

330 increasing T-R separation as they travel further distances with  
 331 more power spreading. In summary, the unwanted reflections  
 332 from the transceiver electronics will have a profound impact on  
 333 the channel, and attenuating these reflected signals below cer-  
 334 tain threshold could be an important issue when building the  
 335 transceiver systems.

#### 336 IV. CHARACTERIZATION OF D-BAND OLOS CHANNEL

##### 337 A. OLoS Path Loss and Shadowing

338 The OLoS environment is created by placing a glass beaker,  
 339 a plastic cup, and a ceramic mug in the midpoint of the sepa-  
 340 ration distance, and its top edge is 3.5 cm above the LoS  
 341 path. The measured path losses for these three scenarios and  
 342 three different separation distances are presented in Fig. 9(a)-  
 343 (c), respectively. The measured results are compared with the  
 344 free-space theoretical path loss obtained using (1). The plots  
 345 show that the measured path loss is much higher than the free-  
 346 space path loss, which is an expected result since the OLoS has  
 347 higher losses due to obstructions in LoS. Furthermore, we can  
 348 observe that the plastic cup introduces the least amount of atten-  
 349 uation compared to free-space path loss and that the variation  
 350 of path loss across frequencies is minimal. The glass beaker  
 351 introduces higher attenuation and as the distance increases, the  
 352 path loss variations as the function of frequency become more  
 353 pronounced. Finally, the ceramic mug introduces the high-  
 354 est attenuation and the path loss variations as the function  
 355 of frequency become dominant. We can observe that ceramic  
 356 material introduces similar attenuation as a glass at lower fre-  
 357 quencies, i.e., 110–130 GHz, but then the loss increases to over  
 358 100 dB in the range of 140–160 GHz. We can also observe

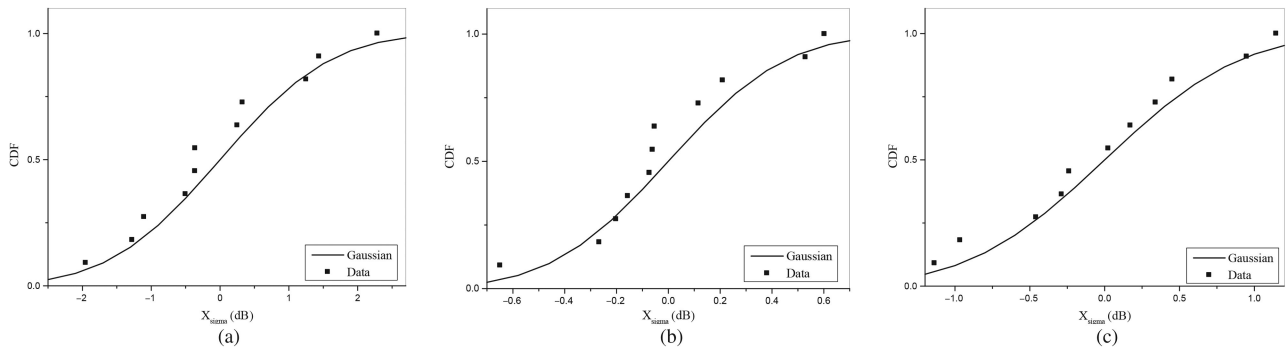
T3:1 TABLE III  
 T3:2 LOG-DISTANCE PATH LOSS MODEL PARAMETERS

	OLOS		
	Glass beaker	Plastic cup	Ceramic mug
Path loss exponent, $\gamma$	2.9519	1.8964	2.1356
Std. deviation, $\sigma$ (dB)	1.3418	0.3757	1.3746
Path loss at $d_0=1\text{m}$ , $PL_0$ (dB)	84.88	77.32	87.94

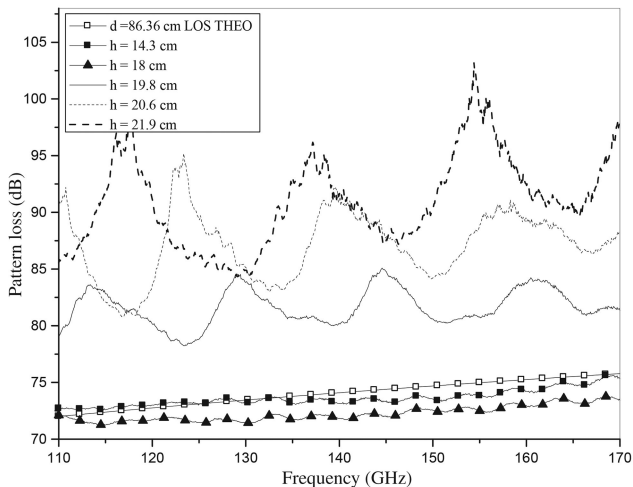
that the maximum of the path loss changes with the separation  
 between the  $T_x$  and  $R_x$ .

Fig. 9(d)–(f) shows the scatter plot of the path loss as a func-  
 tion of T-R separation for glass, plastic, and ceramic OLoS  
 environments, respectively. All 11 distances are used for the  
 scatter plot to obtain the best linear regression fit. As in the  
 LoS case, there are minimal discrepancies among ten consecu-  
 tive measurements because the channel is quasi-static with no  
 moving objects in the environment.

To estimate the path-loss model parameters  $\gamma$  and  $\sigma$  (dB)  
 in (3), we have performed the least-squares linear regression  
 fitting through the scatter of measured path loss points and  
 the results are shown in Fig. 9(d)–(f) for glass, plastic, and  
 ceramic, respectively. The path loss exponents ( $\gamma$ ), standard  
 deviations ( $\sigma$ ), and the path losses at reference distance, 1 m,  
 ( $PL_0$ ) for all three obstruction materials are summarized in  
 Table III. We can observe that the path loss exponent of plas-  
 tic cup is the closest to the LoS path loss exponent value of  
 1.96, which is not surprising since plastic is very transparent  
 at D-band frequencies. For glass and ceramic, due to the con-  
 siderable blockage of LoS path, the path loss exponents have  
 increased above the free-space value of 2. In OLoS scenarios,  
 shadow fading becomes more dominant because of the presence



F10:1 Fig. 10. Zero-mean Gaussian distributed shadow fading and measured shadow fading for OLoS scenarios. (a) Glass beaker. (b) Plastic cup. (c) Ceramic mug.



F11:1 Fig. 11. Variation in path loss with varying height of the ceramic mug  
F11:2 obstruction.

382 of obstructions. To confirm that shadowing can be modeled  
383 as a zero-mean Gaussian distributed random variable, we have  
384 compared the measured distribution of shadow fading with the  
385 Gaussian distribution in Fig. 10. Table III shows that standard  
386 deviation around the mean path loss is the smallest with plastic  
387 obstruction and similar (but much higher) for glass and ceramic  
388 obstructions.

389 Fig. 11 shows variation in OLoS path loss with varying  
390 height of the obstruction, while the T-R separation is fixed at  
391 86.36 cm. As described in Section II-C, the LoS is 20.6 cm  
392 above the table, while  $h$  is varied from 14.3 to 21.9 cm. In  
393 Fig. 11, we can see that the path loss closely follows the  
394 theoretical free-space path loss curve when the LoS path is  
395 clear of obstruction, which corresponds to  $h = 14.3$  cm in the  
396 figure. One interesting observation here is that the path loss  
397 curve for  $h = 18$  cm is about 2 dB below the free-space curve.  
398 Geometrical optics simulations reveal that the ceramic mug  
399 height of 18 cm at separation distance of 86.36 cm places the  
400 top rim of the mug on the boundary of the beam. This results  
401 in the second ray that reflects off the mug's top edge, which  
402 combines vectorially with the first LoS path, leading to a slight  
403 gain in the received power, and therefore slightly lower path  
404 loss than predicted by (1). On the other hand, as  $h$  increases, or  
405 as the mug obstructs more of the LoS path, it is observed that  
406 the path loss increases and becomes more frequency-dependent

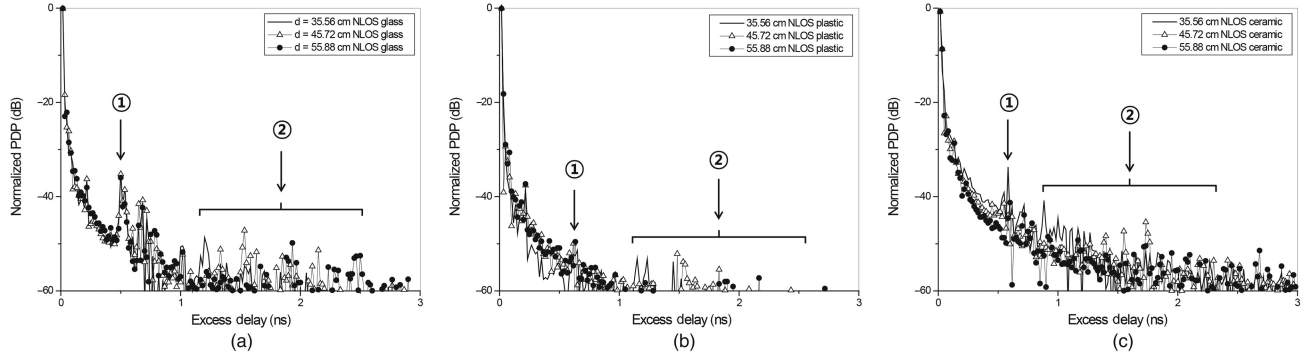
with higher peaks. For this case, our experimental results and  
407 application of uniform geometrical theory of diffraction (UTD)  
408 have revealed the presence of diffraction at the convex surface of the  
409 cylindrical obstruction. The creeping waves or the surface-diffracted  
410 rays that travel around the cylinder in clockwise and counter-clock-  
411 wise directions and their interference seem to be causing the variation  
412 in the measured  $S_{21}$ . Further characterization of this particular  
413 OLoS channel is one of our main future works.  
414  
415

### B. OLoS Multipath Characterization

416  
417 Fig. 12 plots the PDPs for three obstructions: glass, plastic,  
418 and ceramics, respectively. We can observe that all three  
419 PDPs have two distinct segments: one where the reflection peak  
420 appears at the same time delay regardless of the T-R separation  
421 distance (shown as 1 in the figures), followed by the reflection  
422 peaks whose positions depend on the T-R separation distance  
423 (shown as 2 in the figures). Here, we note that the difference  
424 between the first and the second arriving path is always equal  
425 to twice the cup diameter, regardless of the T-R separation  
426 distance, which explains why the multipath marked as 1 appears at  
427 the same excess delay for all distances. Furthermore, from the  
428 excess delay that corresponds to the first multipath (marked as 1  
429 in the figures), we can conclude that this multipath corresponds  
430 to a ray that penetrated the cup, reflected off the wall closer to  
431 the  $R_x$ , reflected off the wall closer to the  $T_x$ , and traveled out-  
432 side the cup to the  $R_x$ . Although the higher order of reflections  
433 might be present, the  $R_x$  sensitivity is not high enough to detect  
434 them.

435 From Fig. 12, we can observe that the PDP for the plastic cup  
436 has weaker reflected paths compared to the glass and ceramic  
437 mugs because most of the energy goes through the plastics and  
438 does not stay trapped inside the obstruction. Furthermore, we  
439 can observe that the PDP for the ceramic mug has significant  
440 reflections only at the distance of 35.56 cm, whereas for 45.72  
441 and 55.88 cm, it is difficult to identify them because the reflec-  
442 tions are significantly attenuated due to material properties.

443 In the PDP section marked as 2 in Fig. 12(a)–(c), we can  
444 observe that the position of the multipath peak depends on the  
445 T-R separation. From the excess delay that corresponds to the  
446 second multipath, we can deduce that the signal has traveled  
447 through the obstruction, was reflected from the  $R_x$  probe head,  
448 was reflected once more off the obstruction, and then received



F12:1 Fig. 12. PDPs for OLoS scenarios. (a) Glass beaker. (b) Plastic cup. (c) Ceramic mug.

T4:1  
T4:2  
T4:3

TABLE IV  
MEAN EXCESS DELAY, RMS DELAY SPREAD, AND COHERENCE  
BANDWIDTH FOR DIFFERENT OBSTRUCTION MATERIALS

d (cm)	Glass beaker			Plastic cup			Ceramic mug		
	$\tau_m$ (ps)	$\tau_{rms}$ (ps)	$B_c$ (GHz)	$\tau_m$ (ps)	$\tau_{rms}$ (ps)	$B_c$ (GHz)	$\tau_m$ (ps)	$\tau_{rms}$ (ps)	$B_c$ (GHz)
35.56	18.06	31.90	4.99	17.03	14.52	10.96	22.21	76.60	2.08
55.88	18.31	45.63	3.49	17.42	23.90	6.66	21.48	62.93	2.53
76.2	18.72	57.19	2.78	16.79	10.85	14.68	20.42	54.98	2.89

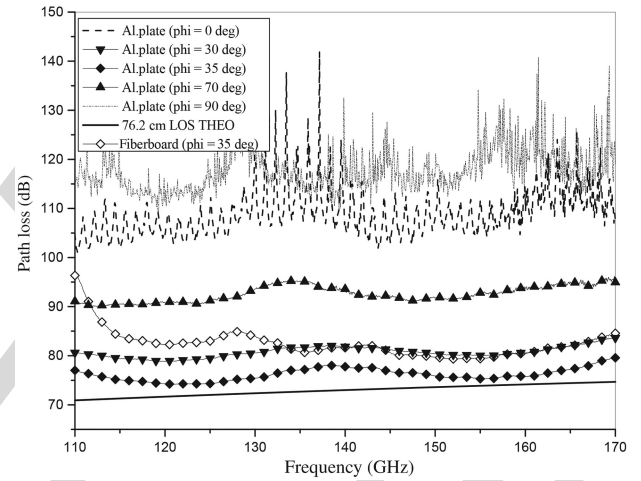
449 by the  $R_x$  antenna. Alternatively, the signal was reflected off  
450 obstruction, then reflected back from the  $T_x$  probe head, and  
451 then traveled through obstruction to the  $R_x$ .

452 Note that the width of the main peak (first arriving path) is the  
453 widest for ceramic mug, which is followed by glass beaker and  
454 plastic cup, as observed in Fig. 12. This indicates that the ratio  
455 of the power associated with the strongest first arriving path to  
456 that of the following reflected paths is the highest for plastic,  
457 while the ratio is the lowest for ceramic. This agrees with the  
458 fact that **glass** is the most transparent to the waves, allowing  
459 most of the transmitted rays to pass through without multiple  
460 reflections. For ceramics, on the other hand, the transparency of  
461 the material is much lower than glass, which gives rise to more  
462 reflected paths that arrive with delays that are very close to each  
463 other. This high temporal proximity is manifested as clustering  
464 of the reflected paths, which leads to pulse broadening as shown  
465 in Fig. 12(c).

466 The multipath characterization parameters,  $\tau_m$ ,  $\tau_{rms}$ , and  $B_c$ ,  
467 in the OLoS environment with the three different obstructions  
468 for the three T-R spacings, 35.56, 55.88, and 76.2 cm, are  
469 summarized in Table IV. The OLoS channel obstructed by  
470 the plastic cup has the largest coherence bandwidth of almost  
471 11 GHz at 35.56 cm, which is comparable with that of LoS  
472 environment for the same distance. Meanwhile, much narrower  
473 coherence bandwidths below 5 GHz are observed for glass and  
474 ceramic mug obstructions.

#### 475 V. CHARACTERIZATION OF D-BAND RNLOS CHANNEL

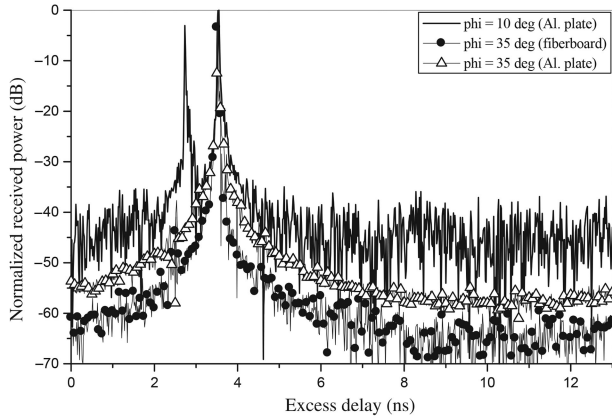
476 Another possible way of communication is through RNLoS  
477 paths. Since the effectiveness of communication will depend  
478 on the reflectivity of the material; here, we compare two dif-  
479 ferent reflectors: aluminum plate and fiberboard. Furthermore,  
480 we investigate the effect of angular orientation of the  $R_x$  on the



F13:1 Fig. 13. Measured RNLoS path loss for different  $R_x$  angles with aluminum  
F13:2 plate, measured RNLoS path loss with fiberboard, and the theoretical free-space  
F13:3 path loss for  $d = 76.2$  cm.

481 received power levels. The  $T_x$  is fixed at  $\phi_T = 35^\circ$ , and the  $R_x$   
482 is rotated between  $\phi_R = 0^\circ$  and  $\phi_R = 90^\circ$ . The angles are mea-  
483 sured from the direct LoS path. The T-R separation distance  
484 has been fixed at  $d = 76.2$  cm. The measured and theoretical  
485 (free-space) path loss for several angles  $\phi_R$  with aluminum  
486 plate and fiberboard as reflectors are shown in Fig. 13. It is  
487 evident from the figure that the level of received power is closest  
488 to the theoretical LoS level when  $\phi_R = \phi_T = 35^\circ$ , since  
489 the condition  $\phi_R = \phi_T$  ensures that the maximum power is  
490 transferred through specular reflection. The slight discrepancy  
491 from the LoS level can be attributed to the reflection coefficient  
492 of the aluminum plate. As the  $R_x$  angle  $\phi_R$ , deviates from  
493  $35^\circ$ , it is observed that reception becomes weaker and the path  
494 loss significantly increases. At the two extremes,  $\phi = 0^\circ$  and  
495  $\phi = 90^\circ$ , we can observe that the communication is essentially  
496 lost. Furthermore, we can observe that the path loss is higher  
497 when the fiberboard is used as the reflector. This is not surpris-  
498 ing result because the fiberboard has lower reflectivity and  
499 higher surface roughness.

500 The PDPs for RNLoS channel with aluminum plate and  
501 fiberboard as the reflector for the angular positions,  $\phi_R = 10^\circ$   
502 and  $35^\circ$  are presented in Fig. 14. The peaks that coincide at  
503  $\tau = 3.6$  ns represent the paths bouncing off the reflector, while  
504 an additional peak at  $\tau = 2.7$  ns observed for  $\phi_R = 10^\circ$  is a



F14:1 Fig. 14. PDP for different  $R_x$  angles with aluminum plate and fiberboard as  
 F14:2 the reflecting surfaces.

T5:1 TABLE V  
 T5:2 MEAN EXCESS DELAY, RMS DELAY SPREAD, AND COHERENCE  
 T5:3 BANDWIDTH FOR DIFFERENT  $R_x$  ANGULAR POSITIONS

$\Phi_R$ ( $^\circ$ )	Aluminum plate			Cardboard		
	$\tau_m$ (ps)	$\tau_{rms}$ (ps)	$B_c$ (GHz)	$\tau_m$ (ps)	$\tau_{rms}$ (ps)	$B_c$ (GHz)
0	65.72	312.89	0.51	–	–	–
10	89.14	311.20	0.51	–	–	–
35	17.07	9.36	17.00	18.18	36.84	4.32
60	17.17	26.97	5.90	–	–	–
90	132.36	678.48	0.23	–	–	–

505 result of the direct LoS path that arrives before the reflected  
 506 path. Note that for the same  $R_x$  angle of  $\phi_R = 35^\circ$ , alu-  
 507 minium plate and fiberboard produce similar PDPs with a single  
 508 reflected path and no higher order reflections due to the high  
 509 directivity of the antenna.

510 Table V presents the mean excess delay, rms delay spread,  
 511 and coherence bandwidth for several  $R_x$  angular positions in  
 512 RNLoS environment. As expected, we can observe the largest  
 513 coherence bandwidth for  $\phi_R = 35^\circ$ , at which maximum power  
 514 transfer occurs. At the same angle, when the reflecting surface  
 515 is fiberboard, the coherence bandwidth is four times smaller. It  
 516 is also observed that the coherence bandwidth reduces rapidly  
 517 as the  $R_x$  angle deviates from  $35^\circ$ , dropping to megahertz range  
 518 at  $\phi_R = 90^\circ$ .

## 519 VI. CONCLUSION

520 This paper presents measurements and characterization of  
 521 D-band indoor channels. The measurements are performed in  
 522 LoS, OLoS, and RNLoS environments. For OLoS scenario,  
 523 cylindrical objects of different materials are used as obstruc-  
 524 tions. For RNLoS, different surfaces are used as reflectors.  
 525 From the large set of LoS and OLoS measured data, the param-  
 526 eters for single-slope path loss model with shadowing are  
 527 devised. Furthermore, the analysis of multipath propagation is  
 528 performed. The rms delay spread, the mean excess delay, and  
 529 the coherence bandwidth for LoS, OLoS, and RNLoS environ-  
 530 nments are calculated. In addition, the PDPs for LoS, OLoS,  
 531 and RNLoS environments are analyzed. The results show that  
 532 strong multiple reflections from the  $T_x$  and  $R_x$  electronics are

present both in LoS and OLoS environments. Additionally, the  
 results show that glass and ceramic objects in the propaga-  
 tion path produce surface-diffracted rays which clock-wise and  
 counter-clock-wise superposition leads to frequency-dependent  
 path loss. Finally, the results show that the RNLoS measured  
 path loss with aluminum plate as a reflector is very similar to  
 free-space path loss when the angle of incidence and the angle  
 of reflection are equal.

## REFERENCES

- [1] S. Chery, "Edholm's law of bandwidth," *IEEE Spectrum*, vol. 41, no. 7, pp. 58–60, Jul. 2004.
- [2] P. Smulders, "Exploiting the 60 GHz band for local wireless multimedia access: Prospects and future directions," *IEEE Commun. Mag.*, vol. 40, no. 1, pp. 140–147, Aug. 2002.
- [3] M. Fryziel, C. Loyez, L. Clavier, N. Rolland, and P. A. Rolland, "Path-loss model of the 60-GHz indoor radio channel," *Microw. Opt. Technol. Lett.*, vol. 34, no. 3, pp. 158–162, 2002.
- [4] H. Xu, V. Kukshya, and T. S. Rappaport, "Spatial and temporal characteristics of 60-GHz indoor channels," *IEEE J. Sel. Areas Commun.*, vol. 20, no. 3, pp. 620–630, Apr. 2002.
- [5] N. Moraitis and P. Constantinou, "Indoor channel measurements and characterization at 60 GHz for wireless local area network applications," *IEEE Trans. Antennas Propag.*, vol. 52, no. 12, pp. 3180–3189, Dec. 2004.
- [6] T. Zwick, T. J. Beukema, and H. Nam, "Wideband channel sounder with measurements and model for the 60 GHz indoor radio channel," *IEEE Trans. Veh. Technol.*, vol. 54, no. 4, pp. 1266–1276, Jul. 2005.
- [7] H. Yang, P. F. M. Smulders, and M. H. A. J. Herben, "Indoor channel measurements and analysis in the frequency bands 2 GHz and 60 GHz," in *Proc. IEEE Symp. Pers. Indoor Mob. Radio Commun.*, Sep. 2005, pp. 1–5.
- [8] S. Geng, J. Kivinen, X. Zhao, and P. Vainikainen, "Millimeter-wave propagation channel characterization for short-range wireless communications," *IEEE Trans. Veh. Technol.*, vol. 58, no. 1, pp. 3–13, Jan. 2009.
- [9] M. Peter and W. Keusgen, "Analysis and comparison of indoor wideband radio channels at 5 and 60 GHz," in *Proc. Eur. Conf. Antennas Propag. (EUCAP'09)*, Mar. 2009, pp. 3830–3834.
- [10] T. S. Rappaport *et al.*, "Millimeter wave mobile communications for 5G cellular: It will work!" *IEEE Access*, vol. 1, pp. 335–349, May 2013.
- [11] P. H. Siegel, "Terahertz technology," *IEEE Trans. Microw. Theory Techn.*, vol. 50, no. 3, pp. 910–928, Mar. 2002.
- [12] T. Kleine-Ostmann, K. Pierz, G. Hein, P. Dawson, and M. Koch, "Audio signal transmission over THz communication channel using semiconductor modulator," *Electron. Lett.*, vol. 40, pp. 124–126, Jan. 2004.
- [13] C. Jastrow *et al.*, "300 GHz transmission system," *Electron. Lett.*, vol. 44, pp. 213–215, Jan. 2008.
- [14] C. Jastrow *et al.*, "Wireless digital data transmission at 300 GHz," *Electron. Lett.*, vol. 46, pp. 661–687, Apr. 2010.
- [15] S. Priebe *et al.*, "Channel and propagation measurements at 300 GHz," *IEEE Trans. Antennas Propag.*, vol. 59, no. 5, pp. 1688–1698, May 2011.
- [16] R. Piesiewicz *et al.*, "Short-range ultra-broadband terahertz communications: Concepts and perspectives," *IEEE Antennas Propag. Mag.*, vol. 49, no. 6, pp. 24–39, Jun. 2007.
- [17] R. Piesiewicz *et al.*, "Scattering analysis for the modeling of THz communication systems," *IEEE Trans. Antennas Propag.*, vol. 55, no. 11, pp. 3002–3009, Nov. 2007.
- [18] Y. Yang, M. Mandehgar, and D. Grischkowsky, "Broadband THz pulse transmission through the atmosphere," *IEEE Trans. Terahertz Sci. Technol.*, vol. 1, no. 1, pp. 264–273, Sep. 2011.
- [19] J. M. Jornet and I. F. Akyildiz, "Channel modeling and capacity analysis for electromagnetic wireless nanonetworks in the terahertz band," *IEEE Transactions on Wireless Communications*, vol. 10, no. 10, pp. 3211–3221, Oct. 2011.
- [20] R. Piesiewicz *et al.*, "Terahertz characterisation of building materials," *IEEE Electron. Lett.*, vol. 41, no. 18, pp. 1002–1004, Sep. 2005.
- [21] C. Jansen, R. Piesiewicz, D. Mittleman, T. Kürner, and M. Koch, "The impact of reflections from stratified building materials on the wave propagation in future indoor terahertz communication systems," *IEEE Trans. Antennas Propag.*, vol. 56, no. 5, pp. 1413–1419, May 2008.

- [22] S. Priebe *et al.*, "A comparison of indoor channel measurements and ray tracing simulations at 300 GHz," in *Proc. Int. Conf. Infrared Millim. Terahertz Waves (IRMMW-THz)*, Sep. 2010.
- [23] M. Jacob *et al.*, "Diffraction in mm and sub-mm wave indoor propagation channels," *IEEE Trans. Microw. Theory Techn.*, vol. 60, no. 3, pp. 833–844, Mar. 2012.
- [24] S. Kim and A. Zajić, "Path loss model for 300-GHz wireless channels," in *Proc. IEEE Int. Symp. Antennas Propag.*, Memphis, Tennessee, USA, Jul. 2014, pp. 1–2.
- [25] S. Kim and A. Zajić, "Statistical characterization of 300-GHz propagation on a desktop," *IEEE Trans. Veh. Technol.*, to be published.
- [26] T. Kosugi *et al.*, "120-GHz Tx/Rx waveguide modules for 10-Gbit/s wireless link system," in *Proc. IEEE CSICS Dig.*, Oct. 2006, pp. 25–28.
- [27] I. Sarkas, E. Laskin, J. Hasch, P. Chevalier, and S. P. Voinigescu, "Second generation transceivers for D-band radar and data communication applications," in *Proc. IEEE IMS Dig.*, May 2010, pp. 1328–1331.
- [28] E. Laskin *et al.*, "Nanoscale CMOS transceiver design in the 90–170 GHz range," *IEEE Trans. Microw. Theory Techn.*, vol. 57, no. 12, pp. 3477–3490, Dec. 2009.
- [29] G. Liu and E. K. Seo, "Detecting snowfall over land by satellite high-frequency microwave observations: The lack of scattering signature and a statistical approach," *J. Geophys. Res.: Atmos.*, vol. 118, pp. 1376–1387, Feb. 2013.
- [30] Z. Chen and J. C. Cao, "Channel characterization at 120 GHz for future indoor communication systems," *Chin. Phys. B*, vol. 22, no. 5, p. 059201, 2013.
- [31] A. Zajić, *Mobile-to-Mobile Wireless Channels*. Norwood, MA, USA: Artech House, Jan. 2013.



Mitel Networks, Kanata, ON, Canada.

**Seunghwan Kim** (S'14) was born in Seoul, South Korea, in 1986. He received the Bachelor of Applied Science degree in electrical engineering from the University of Waterloo, Waterloo, ON, Canada, in 2009. He is currently pursuing the Ph.D. degree in electrical engineering at Georgia Institute of Technology, Atlanta, GA, USA.

During his degree, he worked as a Research Assistant with the Telecommunication Group, Korea Electrotechnology Research Institute (KERI), Changwon, Korea, and as a Hardware Engineer with



an Assistant Professor with the Department of Electrical Engineering, Lahore University of Management Sciences, Lahore, Pakistan. He has authored/coauthored more than 35 research papers in peer-reviewed conferences and journals. His research interests include the RF and microwave system design, millimeter wave circuit and package design, multilayer organic packaging, on-chip and off-chip antenna design, and phased array systems.

Dr. Khan has been the publications Chair for four IEEE conferences: RWS, PAWR, WisNet, and BioWireSS, since 2010. Since 2011, he has also been a Technical Program Committee (TPC) member for IEEE Radio and Wireless Symposium (RWS). He was the recipient of a MS leading to Ph.D. fullbright Scholarship.



**Alenka Zajić** (S'99–M'09–SM'13) received the B.Sc. and M.Sc. degrees in electrical engineering from the University of Belgrade, Belgrade, Serbia, in 2001 and 2003, respectively, and the Ph.D. degree in electrical and computer engineering from Georgia Institute of Technology, Atlanta, GA, USA, in 2008.

Currently, she is an Assistant Professor with the School of Electrical and Computer Engineering, Georgia Institute of Technology. Prior to that, she was a Visiting Faculty at the School of Computer Science, Georgia Institute of Technology, a Postdoctoral Fellow with the Naval Research Laboratory, and Design Engineer with Skyworks Solutions Inc. Her research interests include electromagnetics, wireless communications, signal processing, and computer engineering.

Dr. Zajić was the recipient of the Neal Shepherd Memorial Best Propagation Paper Award, the Best Paper Award at ICT 2008, the Best Student Paper Award at WCNC 2007, the Dan Noble Fellowship in 2004, awarded by Motorola Inc., and the IEEE VEHICULAR TECHNOLOGY SOCIETY for quality impact in the area of vehicular technology. Currently, she is an Editor for IEEE TRANSACTIONS ON WIRELESS COMMUNICATIONS and the Chair of the IEEE MTT/AP Atlanta Chapter.



**John Papapolymerou** (F'xx) received the B.S.E.E. degree from the National Technical University of Athens, Athens, Greece, in 1993, and the M.S.E.E. and Ph.D. degrees from the University of Michigan, Ann Arbor, MI, USA, in 1994 and 1999, respectively.

From 1999 to 2001, he was an Assistant Professor with the Department of Electrical and Computer Engineering, University of Arizona, Tucson, AZ, USA, and during 2000 and 2003, he was a Visiting Professor at the University of Limoges, Limoges, France. From 2001 to 2005 and 2005 to 2009, he was an Assistant Professor and Associate Professor, respectively, with the School of Electrical and Computer Engineering, Georgia Institute of Technology, Atlanta, GA, USA, where he is currently the Ken Byers Professor. He has authored or coauthored over 350 publications in peer-reviewed journals and conferences. His research interests include the implementation of micromachining techniques and MEMS devices in microwave, millimeter-wave and THz circuits and the development of both passive and active planar circuits and antennas on semiconductor (Si/SiGe, GaAs) and organic substrates (liquid crystal polymer-LCP, LTCC) for system-on-a-chip (SOC)/ system-on-a-package (SOP) RF front ends.

Dr. Papapolymerou currently serves as Editor-in-Chief for IEEE MICROWAVE AND WIRELESS COMPONENTS LETTERS (MWCL). He has also served as an Associate Editor for IEEE TRANSACTIONS ON MICROWAVE THEORY AND TECHNIQUES from 2010 to 2012, and as Chair for Commission D of the US National Committee of URSI from 2009 to 2011. He was also an Associate Editor for IEEE MWCL (2004–2007), and IEEE TRANSACTIONS ON ANTENNAS AND PROPAGATION (2004–2010). During 2004, he was the Chair of the IEEE MTT/AP Atlanta Chapter. He was the recipient of the 2012 IEEE ANTENNAS AND PROPAGATION SOCIETY (AP-S) H.A. Wheeler Prize Paper Award, the 2010 IEEE AP-S John Kraus Antenna Award, the 2009 IEEE MICROWAVE THEORY AND TECHNIQUES-SOCIETY (MTT-S) Outstanding Young Engineer Award, the 2009 School of ECE Outstanding Junior Faculty Award, the 2004 Army Research Office (ARO) Young Investigator Award, the 2002 National Science Foundation (NSF) CAREER award, the Best Paper Award at the 3rd IEEE International Conference on Microwave and Millimeter-Wave Technology (ICMMT2002), Beijing, China, and the 1997 Outstanding Graduate Student Instructional Assistant Award presented by the American Society for Engineering Education (ASEE), the University of Michigan Chapter.

## QUERIES

- Q1: Please provide issue number for Ref. [10].
- Q2: Please provide page range for Ref. [22].
- Q3: Please update Ref. [25].
- Q4: Please provide field of studies for “B.S.E.E., M.S.E.E., and Ph.D.” degrees and membership history (year) of author “John Papapolymerou.”

IEEE  
Proof

# D-Band Channel Measurements and Characterization for Indoor Applications

Seunghwan Kim, *Student Member, IEEE*, Wasif Tanveer Khan, *Member, IEEE*,  
Alenka Zajić, *Senior Member, IEEE*, and John Papapolymerou, *Fellow, IEEE*

**Abstract**—This paper presents measurements and characterization of D-band indoor channels. The measurements are performed in line-of-sight (LoS), obstructed-LoS (OLOs), and reflected non-LoS (RNLoS) environments. For OLoS scenario, cylindrical objects of different materials are used as an obstruction. For RNLoS, different surfaces are used as reflectors. From the large set of LoS and OLoS measured data, the parameters for single-slope path loss model with shadowing are devised. Furthermore, the analysis of multipath propagation is performed. The results show that strong multiple reflections from the transmitter and receiver electronics are present both in LoS and OLoS environments. Additionally, the results show that glass and ceramic objects in the propagation path produce surface-diffracted rays which clock-wise and counter clock-wise superposition leads to frequency-dependent path loss. Finally, the results show that the RNLoS measured path loss with aluminum plate as a reflector is very similar to free-space path loss when the angle of incidence and the angle of reflection are equal.

**Index Terms**—Channel measurements, channel modeling, D-band channels, indoor channels.

## I. INTRODUCTION

ULTRA-WIDEBAND wireless communication systems are expected to help satisfy the ever-growing need for smaller devices that can offer higher speed wireless communications anywhere and anytime. In the past years, it has become obvious that wireless data rates exceeding 10 Gb/s will be required in several years from now [1]. To achieve this goal, several frequency bands have been explored. For example, propagation characteristics of 60 GHz with an unregulated bandwidth of 7 GHz have been presented in [2]–[10] and references therein. Similarly, propagation characteristics of 300 GHz with an unregulated bandwidth of 47 GHz have been presented in [11]–[25] and references therein. While 60-GHz communications have limited bandwidth, 300 GHz communications are limited in range.

As an alternative, the 60 GHz of spectrum from 110 to 170 GHz (D-band) offers a promising approach to provide

Manuscript received October 22, 2014; revised January 29, 2015; accepted April 02, 2015.

S. Kim, A. Zajić, and J. Papapolymerou are with the School of Electrical and Computer Engineering, Georgia Institute of Technology, Atlanta, GA 30332 USA (e-mail: skim745@gatech.edu; alenka.zajic@ece.gatech.edu; john.papapolymerou@ece.gatech.edu).

W. Khan is with the School of Electrical Engineering, Lahore University of Management Sciences (LUMS), Lahore 54792, Pakistan (e-mail: wasif.tanveer@lums.edu.pk).

Color versions of one or more of the figures in this paper are available online at <http://ieeexplore.ieee.org>.

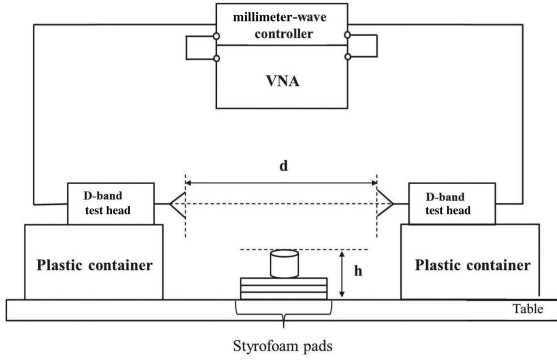
Digital Object Identifier 10.1109/TAP.2015.2426831

sufficient bandwidth and range required for ultra-fast and ultra-wideband data transmissions [26]. This frequency band is ideally suited for short- and medium-range communications. This large bandwidth paired with higher speed wireless links has potential applications in precision positioning and velocity sensors [27], passive millimeter-wave cameras [28] and can open the door to a large number of novel applications such as ultra-high-speed pico-cell cellular links, wireless short-range communications, and on-body communication for health monitoring systems. Note that this frequency band is currently unregulated for wireless communications, and is typically used for atmospheric applications.

To enable wireless communications in D-band, it is imperative to understand propagation mechanisms that govern communication at these frequencies. While D-band has been extensively used for microwave atmospheric sounding (e.g., [29]), to the best of our knowledge, *no indoor D-band* channel characterization based on measurements has been reported in the open literature. Although channel characterization at 120 GHz for an indoor office scenario has been reported in [30], the work only presents ray-tracing simulation results without channel measurements. While atmospheric absorption is the main focus of microwave atmospheric sounding, this loss plays minor role in indoor propagation. Reflections, diffraction, and scattering are more prevalent propagation mechanisms in indoor D-band channels.

As the first step toward characterizing D-band channel, we have performed line-of-sight (LoS), obstructed-LoS (OLOs), and reflected non-LoS (RNLoS) measurements at 140 with 60 GHz of bandwidth between the transmitter ( $T_x$ ) and the receiver ( $R_x$ ). The contributions of this paper are as follows.

- 1) Devised parameters for the single-slope path loss model with shadowing for LoS and OLoS environments. The results show that the path loss exponent is around 1.9 for LoS environment and the variations due to shadowing are negligible. Furthermore, the results show that the path loss exponent for plastic cup OLoS path is the closest to the LoS path loss exponent and that glass and ceramic OLoS path loss exponents increase to 3. Additionally, we find that glass and ceramics objects in the propagation path cause multiple strong reflections leading to higher frequency-dependent path loss. Finally, we observe that the RNLoS path loss with aluminum plate as a reflector is very similar to free-space path loss when the angle of incidence and reflection are equal. This indicates that communication is possible in RNLoS scenarios.



F1:1 Fig. 1. 110–170 GHz measurement setup.

TABLE I  
MEASUREMENT PARAMETERS

Parameter	Symbol	Value
Measurement points	N	801
Intermediate frequency bandwidth	$\Delta f_{IF}$	100 Hz
Average noise floor	$P_N$	-85 dBm
Input signal power	$P_{in}$	0 dBm
Start frequency	$f_{start}$	110 GHz
Stop frequency	$f_{stop}$	170 GHz
Bandwidth	B	60 GHz
Time domain resolution	$\Delta t$	0.0167 ns
Maximum excess delay	$\tau_m$	13 ns

T1:1  
T1:2

- 88 2) Analyzed the rms delay spread  $\tau_{RMS}$ , the mean excess  
 89 delay  $\tau_m$ , and the coherence bandwidth for LoS, OLoS,  
 90 and RNLoS environments. In LoS environment, the mean  
 91 values of  $\tau_{RMS}$  and  $\tau_m$  are 12.84 and 16.95 ps, respec-  
 92 tively. The mean excess delay increases in the presence  
 93 of obstructions, with the smallest increase in the presence  
 94 of plastic cup and the largest increase in the presence of  
 95 ceramic mug. There is almost no increase in the mean  
 96 excess delay in RNLoS environment for aluminum plate  
 97 as a reflector and the equal angles of incidence and  
 98 reflection.
- 99 3) Analyzed the power delay profiles (PDPs) for LoS, OLoS,  
 100 and RNLoS environments. We can observe that the strong  
 101 reflections from the  $T_x$  and  $R_x$  electronics are present  
 102 both in LoS and OLoS environments. Additionally, OLoS  
 103 channels with obstructions of cylindrical shape, such  
 104 as a glass beaker, a plastic cup, or a ceramic mug,  
 105 also experience the diffraction at the convex surface of  
 106 the cylindrical obstruction. The creeping waves, or the  
 107 surface-diffracted rays that travel around the cylinder in  
 108 clock-wise and counter clock-wise directions superim-  
 109 pose leading to frequency dependant path loss.

110 The remainder of this paper is organized as follows.  
 111 Section II describes the measurement equipment, antennas used  
 112 in the measurements, and the measurement setup. Section III  
 113 presents the path loss, shadowing, and multipath propagation  
 114 analysis of LoS measured data. Section IV presents the path  
 115 loss, shadowing, and multipath propagation analysis of OLoS  
 116 measured data, while Section V presents the path loss and mul-  
 117 tipath propagation analysis of RNLoS measured data. Finally,  
 118 Section VI provides some concluding remarks.

## 119 II. MEASUREMENT SETUP

### 120 A. Equipment

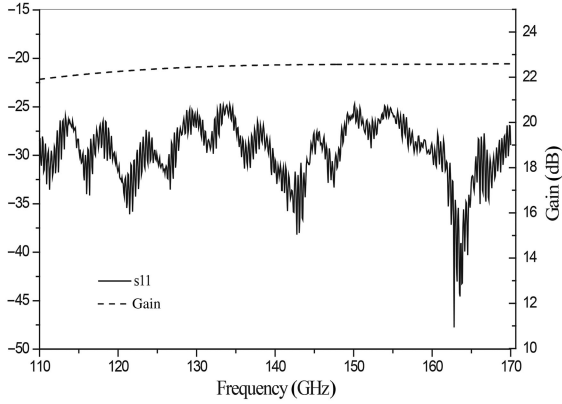
121 The block diagram of the D-band measurement setup is  
 122 shown in Fig. 1. The Agilent E8361C vector network analyzer  
 123 is used for all measurements. The E8361C has a frequency  
 124 range up to 67 GHz; therefore, the N5260A (millimeter-  
 125 wave controller) and OML V06VNA2 (millimeter-wave test  
 126 head modules) are used to extend the range to the D-band

(110–170 GHz). The N5260A millimeter-wave controller  
 127 provides radio frequency (RF) and local oscillator (LO) sig-  
 128 nals to the millimeter-wave test head modules and returns the  
 129 down-converted reference and test IF signals to the VNA for  
 130 process and display. The OML V06VNA2 frequency exten-  
 131 sion module has an LO multiplication factor of 10, which  
 132 up-converts the input LO frequency from 11 to 17 GHz,  
 133 supplied by the millimeter-wave controller, to the D-band  
 134 (110–170 GHz).  
 135

136 The full available bandwidth of 60 GHz is used in all mea-  
 137 surements, which provides the spatial and temporal resolution  
 138 of 5 mm or 0.0167 ns. Due to input power restrictions of the  
 139 mixers, a test signal with a power of 0 dBm is used, provid-  
 140 ing a dynamic range of approximately 90 dB for the chosen  
 141 intermediate frequency filter bandwidth of  $\Delta f_{IF} = 100$  Hz. The  
 142 number of sweep points is set to 801, and the maximum excess  
 143 delay is 13 ns. All measurement parameters are summarized in  
 144 Table I.

### 145 B. Antenna Characteristics

146 The antenna used in the measurement is a pyramidal horn  
 147 with gain that varies from 22 to 23 dBi from 110 to 170 GHz,  
 148 respectively. Both  $T_x$  and  $R_x$  antennas are vertically polar-  
 149 ized and have theoretical half-power beamwidth (HPBW) of  
 150  $12^\circ$  and  $13.5^\circ$  in E- and H-plane, respectively, at 110 GHz.  
 151 The E- and H-plane beamwidths also decrease to  $9^\circ$  and  $12^\circ$ ,  
 152 respectively, toward higher frequencies. Furthermore, antennas  
 153 have sidelobes that are at least 25 dB below the main beam  
 154 and all possible reflectors on the sides of the channel have been  
 155 covered with absorbers as shown in Fig. 3, to ensure that any  
 156 paths resulting from the sidelobes are suppressed. The mea-  
 157 sured  $S_{11}$  and the frequency-dependent gain of the horn antenna  
 158 are presented in Fig. 2. Note that the return loss shown here  
 159 includes the reflections at the interfaces between cable and test  
 160 head, as well as test head and the antenna due to mismatches  
 161 between them. Nevertheless, we can observe that the  $S_{11}$  is  
 162 below  $-25$  dB across the entire bandwidth. In further analy-  
 163 sis, antennas are considered to be part of the channel impulse  
 164 response, which is typically the case in wireless communication  
 165 applications.



F2:1 Fig. 2. Reflection coefficient and gain of the horn antenna used in measure-  
F2:2 ments.

### 166 C. Measurement Scenarios

167 In this measurement campaign, three different scenarios  
168 have been considered: LoS scenario shown in Fig. 3(a), OLoS  
169 scenario shown in Fig. 3(b), and RNLoS scenario shown in  
170 Fig. 3(c).

171 Considering the short-range of D-band applications, the  
172  $T_x$ – $R_x$  separation distance  $d$  shown in Fig. 1, has been varied  
173 from 35.56 (14") to 86.36 cm (34") in 5.08 cm (2") incre-  
174 ments, giving a total of 11 different distances for LoS scenario.  
175 Furthermore, to mitigate the reflections from the ground and the  
176 metallic transceiver cases, the  $T_x$  and  $R_x$  test heads have been  
177 placed on top of a supporting plastic container, and all possible  
178 reflecting surfaces, including the ground, the equipment rack  
179 cabinet, and the front faces of the test heads, have been cover-  
180 ed with absorbers as shown in Fig. 3(a). For OLoS scenario,  
181 obstructions of circular cylinder shape, i.e., cups, have been  
182 used as typical objects present on desk tops. To study the impact  
183 of different materials on propagation in D-band, three different  
184 types of material, i.e., glass, plastic (polystyrene), and ceramic  
185 have been considered. The same 11  $T_x$ – $R_x$  separations as in  
186 LoS scenario have been used for OLoS scenario. Each obstruc-  
187 tion is placed such that the cylinder's center coincides with the  
188 midpoint of the separation distance, and its top edge is 3.5 cm  
189 above the LoS path. Furthermore, to investigate the effect of  
190 obstruction height on path loss, we have varied the positions of  
191 the top rim of the cylinders, or  $h$  in Fig. 1, from 14.3 to 21.9 cm.  
192 The obstruction height has been varied by having different num-  
193 ber of styrofoam pads (which have been tested to cause minimal  
194 reflections at the frequencies of interest) underneath the cylin-  
195 der obstruction, as shown in Fig. 1. Note that the centers of the  
196 horn antennas are located 20.6 cm above the table. Finally, in  
197 RNLoS scenario, we use reflection as the main mechanism of  
198 wave propagation. Two types of reflecting surfaces, aluminum  
199 plate and fiberboard, having different reflectivity and surface  
200 roughness, have been used. Furthermore, by varying the angu-  
201 lar position of the  $R_x$ , while keeping the  $T_x$  position fixed,  
202 the range of  $R_x$  angular offsets at which the  $R_x$  can detect  
203 the reflected signal is studied. For RNLoS, the LoS separation  
204 distance was fixed to 76.2 cm.

## III. CHARACTERIZATION OF D-BAND LOS CHANNEL 205

### A. LoS Path Loss and Shadowing 206

In this paper, we refer to mean path loss as the transmit power  
multiplied by the transmit and receive antenna gains divided by  
the mean received power, i.e.,

$$PL = \frac{P_t \cdot G_t \cdot G_r}{\bar{P}_r} = \left( \frac{4\pi d}{\lambda} \right)^2. \quad (1)$$

The mean path loss is obtained by averaging a swept contin-  
uous wave over time and frequency, i.e.,

$$PL(d) = \frac{1}{MN} \sum_{i=1}^N \sum_{j=1}^M |H(f_i, t_j, d)|^2 \quad (2)$$

where  $H(f_i, t_j, d)$  is the measured complex frequency response  
data matrix,  $N$  is the number of observed frequencies,  $M$  is the  
number of frequency-response snapshots over time, and  $d$  is the  
distance in meters.

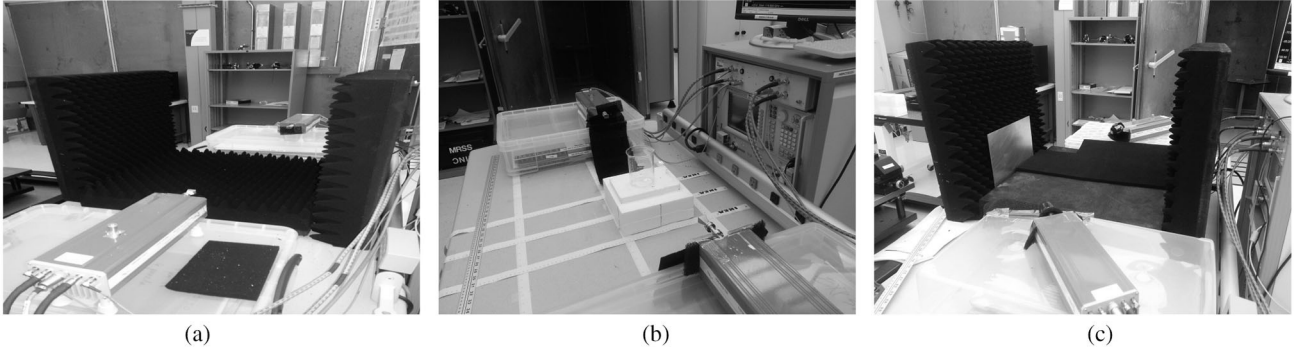
Fig. 4 compares the measured path loss with the theoretical  
path loss calculated using (1). We plot only 5 out of 11 separa-  
tion distances to avoid clutter. We can observe that the measured  
path loss curves very closely follow the theoretical lines. The  
oscillations observed in the path loss curves have been found  
to be a result of multiple reflections between the front faces of  
the  $T_x$  and  $R_x$  test heads. Although they were covered  
with a layer of absorbing material, as shown in Fig. 3(a), it  
was apparently not thick enough to completely mitigate the  
reflections. This resulted in the constructive and destructive  
interference between the direct and reflected rays, which led  
to the oscillation in the measured  $S_{21}$ .

Fig. 5 shows the scatter plot of the mean path loss as a func-  
tion of transmitter–receiver (T–R) separation on a desktop for  
an LoS environment. We can observe that the variation between  
different frequency-response snapshots over time is minimal.  
This is because there are no temporal or spatial variations nor  
additional clutter in the channel that would cause significant  
variations in the measured path loss. Note that this finding is  
significantly different from typical indoor measurements, where  
path loss significantly varies around the mean value. This find-  
ing leads us to conclude that the number of frequency-response  
snapshots over time does not have to be large and we have found  
that ten measurements are sufficient to capture all temporal  
variations in the signal.

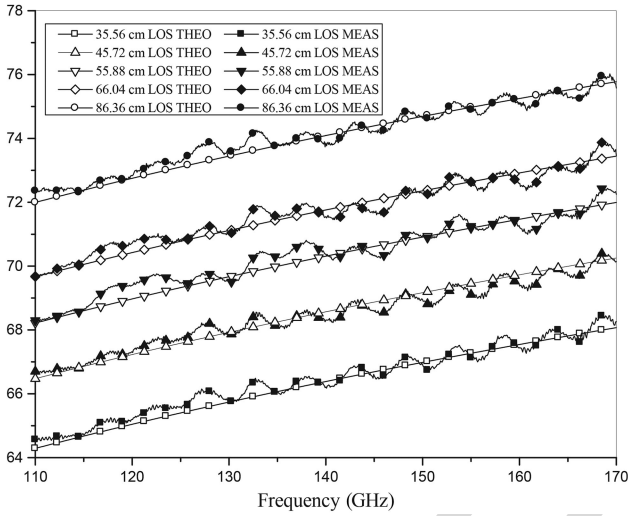
Path loss over distance can be modeled by the path loss  
exponent model [31], i.e.,

$$PL(d) = 10\gamma \log_{10} \left( \frac{d}{d_0} \right) + PL(d_0) + X_\sigma \quad (3)$$

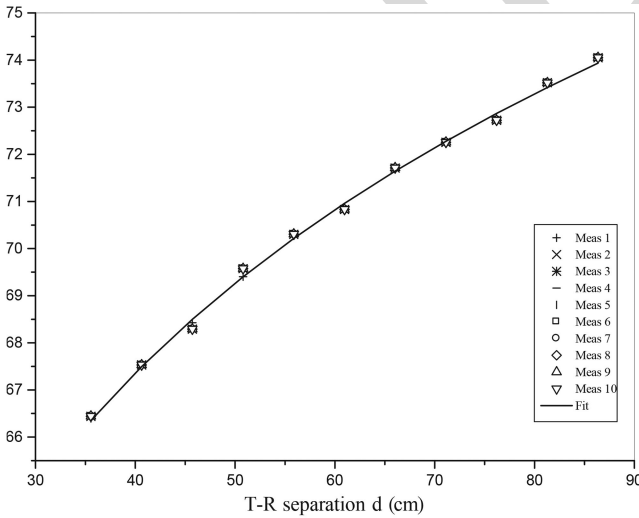
where  $PL(d)$  is the average path loss in dB at the distance  $d$ ,  
 $PL(d_0)$  is the free-space path loss at the reference distance  $d_0$ ,  
 $\gamma$  is the path loss exponent that characterizes how fast the path  
loss increases with the increase in the separation between the  
 $T_x$  and the  $R_x$ , and  $X_\sigma$  represents shadow fading that can be  
modeled as a zero-mean Gaussian distributed random variable  
(in dB) with standard deviation  $\sigma$ . Single slope path loss model



F3:1 Fig. 3. Photographs of measurement scenarios. (a) LoS. (b) OLoS, glass as obstruction. (c) RNLoS, aluminum plate as reflector.

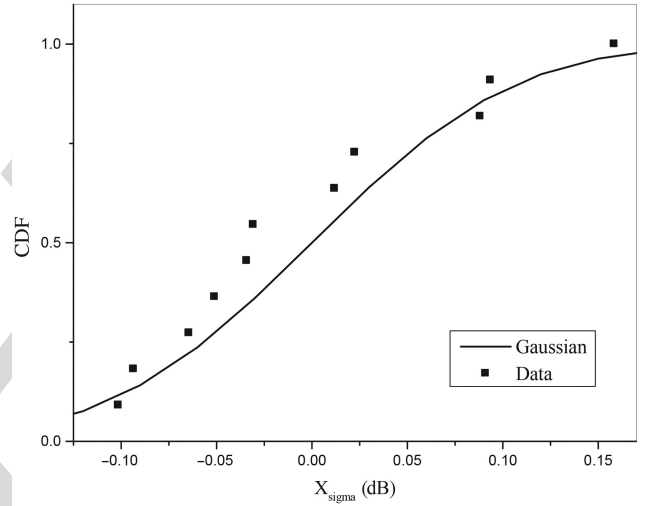


F4:1 Fig. 4. Measured and theoretical path loss for five separation distances.



F5:1 Fig. 5. Scatter plot of the LoS path loss.

250 is a statistical method used to estimate the path-loss slope and  
 251 the variation from the mean path loss. This is an important tool  
 252 when designing communication systems. More advanced statisti-  
 253 cal models can be devised from the measurements if the



F6:1 Fig. 6. Confirming the log-normality of the shadow fading caused by variations  
 F6:2 in T-R alignment in LoS environment.

single slope model does not produce adequate fit, which is not  
 254 the case in our paper. Alternative approach is a deterministic  
 255 approach (e.g., ray-tracing [22] and diffraction modeling [23]),  
 256 which is expected to produce more repeatable results; however,  
 257 it depends on the detailed and accurate description of all objects  
 258 in the propagation space.  
 259

To estimate the path loss model parameters  $\gamma$  and  $\sigma$ (dB)  
 260 in (3), we have performed the least-squares linear regression  
 261 fitting through the scatter of measured path loss points in deci-  
 262 bels such that the root mean square (rms) deviation of path  
 263 loss points about the regression line is minimized. The refer-  
 264 ence distance is  $d_0 = 1$  m and the free-space path loss at the  
 265 reference distance  $d_0$  is  $PL(d_0) = 75.19$  dB. The found path  
 266 loss exponent is around 1.97 and the variations due to shad-  
 267 owing are around  $\sigma = 0.12$  dB. To confirm that shadowing  
 268 can be modeled as a zero-mean Gaussian distributed random  
 269 variable, Fig. 6 compares the measured distribution of shadow  
 270 fading with the Gaussian distribution. This shadowing is due  
 271 to misalignment between the  $T_x$  and  $R_x$  antennas. While this  
 272 may not be a conventional shadowing process, it is still a ran-  
 273 dom process that causes variations of received power at a given  
 274 distance.  
 275

T2:1  
T2:2  
T2:3

TABLE II  
MEAN EXCESS DELAY, RMS DELAY SPREAD, AND COHERENCE  
BANDWIDTH FOR DIFFERENT T-R SEPARATION DISTANCES

d (cm)	Without absorbers			With absorbers		
	$\tau_m$ (ps)	$\tau_{rms}$ (ps)	$B_c$ (GHz)	$\tau_m$ (ps)	$\tau_{rms}$ (ps)	$B_c$ (GHz)
35.56	17.18	32.12	4.95	16.92	12.00	13.26
55.88	17.08	30.50	5.22	16.95	12.84	12.40
76.2	17.04	31.28	5.09	16.87	10.03	15.87

### 276 B. LoS Multipath Characterization

277 Multipath propagation is the propagation mechanism mani-  
278 fested when the transmitted signal reaches the receive antenna  
279 along two or more paths. Such waves typically arrive at the  $R_x$   
280 from many different directions and with different delays, and  
281 combine vectorially at the  $R_x$  antenna. Such channel impulse  
282 response can be characterized as [31]

$$h(t, \tau, d) = \sum_{k=1}^L a_k(t, d) \exp(j\theta_k(t, d)) \delta(t - \tau_k) \quad (4)$$

283 where  $L$  is the number of multipath components,  $a_k$  represents  
284 the amplitude of the  $k$ th multipath component,  $\theta_k$  is the associ-  
285 ated phase, and  $\tau_k$  is the excess delay of the  $k$ th path relative to  
286 the first arrival, and  $\delta(\cdot)$  denotes the Dirac delta function.

287 An estimate of the channel impulse response is made by  
288 taking the inverse discrete Fourier transform (IDFT) of the  
289 measured frequency response. The impulse response is then  
290 normalized such that the area under the squared magnitude  
291 of the power-delay response is equal to one. We refer to a  
292 normalized squared magnitude of the impulse response as the  
293 multipath intensity profile (MIP) at the single point in space.  
294 The noise floor of the MIP is set to 10 dB above the average  
295  $R_x$  noise floor. Part of the MIP characterization is based on  
296 rms delay spread  $\tau_{rms}$ , which is a measure of multipath spread  
297 within the channel. It is an important parameter for characteriz-  
298 ing time dispersion or frequency selectivity. It is the square root  
299 of the second central moment of the MIP and is given by [31]

$$\tau_{rms} = \sqrt{\sum_{k=1}^L (\tau_k - \tau_m)^2 |h(t, \tau_k, d)|^2} \quad (5)$$

300 where  $\tau_m$  is the mean excess delay (the first moment of the  
301 MIP) and is defined as

$$\tau_m = \sum_{k=1}^L \tau_k \cdot |h(t, \tau_k, d)|^2. \quad (6)$$

302 The rms delay spread, mean excess delay, and the coher-  
303 ence bandwidth ( $B_c = 1/(2 \cdot \pi \cdot \tau_{rms})$ ) for three separation  
304 distances with and without the absorbers are presented in  
305 Table II. It is observed that the coherence bandwidths have  
306 almost doubled, or even tripled, when the absorbers are in  
307 place.

308 For the distance of 35.56 cm, the delay spread  $\tau_{rms}$  is  
309 expected to be lower, or equivalently, the coherence bandwidth  
310 is expected to be higher than that of the 76.20 cm, but the

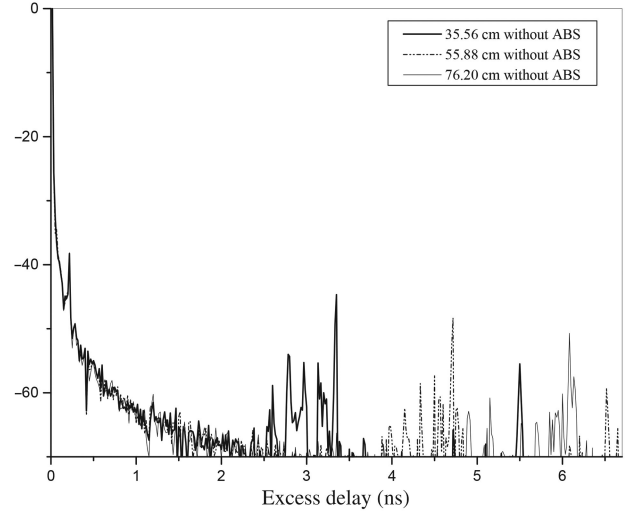


Fig. 7. Normalized PDPs for the three separation distances *without* absorbers. F7:1

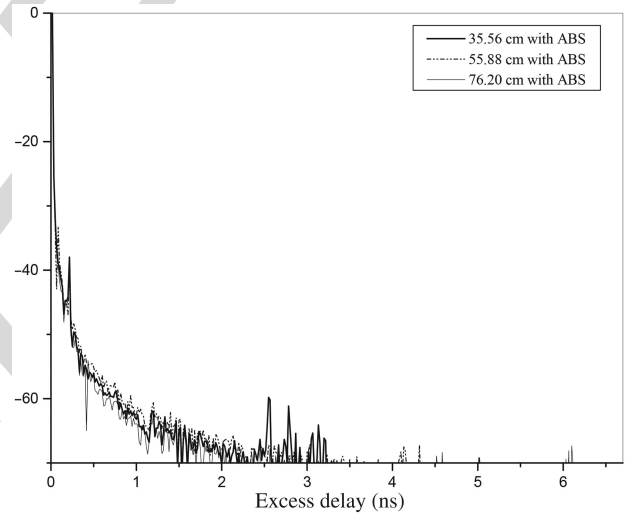
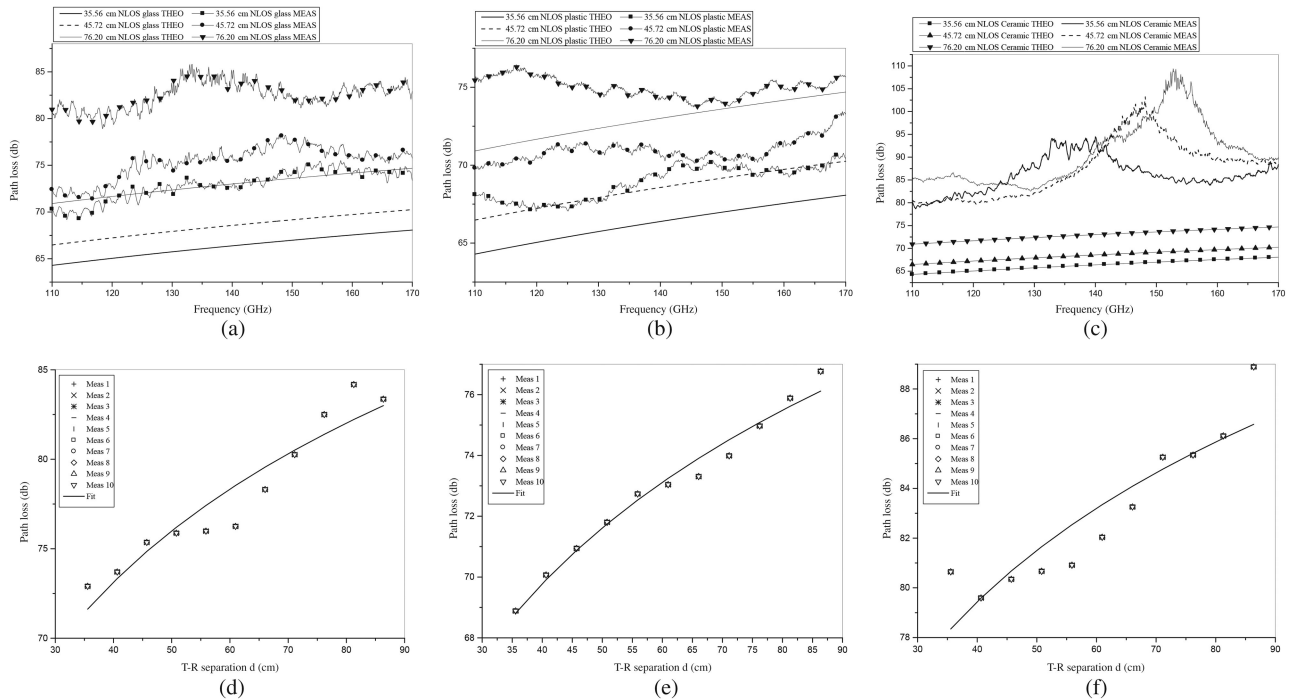


Fig. 8. Normalized PDPs for the three separation distances *with* absorbers. F8:1

311 opposite is observed in Table II. This is because the distance  
312 of 35.56 cm is short enough for the second reflected path to  
313 be captured within the maximum excess delay of 6.67 ns. This  
314 detection of an extra reflected signal results in the increase in  
315 the delay spread, which leads to the decrease in the coherence  
316 bandwidth. When the absorbers are used to cover the  $T_x/R_x$  test  
317 head's front face, we can observe that, while the reflections are  
318 almost completely removed for 76.20 cm, there are still some  
319 weak reflections observed for 35.56 cm. This has again resulted  
320 in a slightly narrower coherence bandwidth for 35.56 cm than  
321 that for 76.20 cm.

322 The PDP of the three separation distances in LoS environ-  
323 ment with and without the absorbers that cover the  $T_x$  and  $R_x$   
324 test heads is shown in Figs. 7 and 8. Note that all PDP's are  
325 normalized, and referenced to the first incoming path. We can  
326 observe that the later arriving paths caused by reflections off the  
327 metallic test head cases can be attenuated using the absorbers. It  
328 is also observed that the reflected paths have increasing excess  
329 delay, more delay spread, and decreasing signal power with



F9:1 Fig. 9. Path loss in OLoS scenario as a function of frequency, where the obstructions are (a) glass beaker; (b) plastic cup; and (c) ceramic mug (upper row) and  
 F9:2 the path loss scatter plot as a function of distance (lower row) for OLoS scenarios, where the obstructions are (d) glass beaker; (e) plastic cup; and (f) ceramic mug.

330 increasing T-R separation as they travel further distances with  
 331 more power spreading. In summary, the unwanted reflections  
 332 from the transceiver electronics will have a profound impact on  
 333 the channel, and attenuating these reflected signals below cer-  
 334 tain threshold could be an important issue when building the  
 335 transceiver systems.

#### 336 IV. CHARACTERIZATION OF D-BAND OLOS CHANNEL

##### 337 A. OLoS Path Loss and Shadowing

338 The OLoS environment is created by placing a glass beaker,  
 339 a plastic cup, and a ceramic mug in the midpoint of the sepa-  
 340 ration distance, and its top edge is 3.5 cm above the LoS  
 341 path. The measured path losses for these three scenarios and  
 342 three different separation distances are presented in Fig. 9(a)-  
 343 (c), respectively. The measured results are compared with the  
 344 free-space theoretical path loss obtained using (1). The plots  
 345 show that the measured path loss is much higher than the free-  
 346 space path loss, which is an expected result since the OLoS has  
 347 higher losses due to obstructions in LoS. Furthermore, we can  
 348 observe that the plastic cup introduces the least amount of atten-  
 349 uation compared to free-space path loss and that the variation  
 350 of path loss across frequencies is minimal. The glass beaker  
 351 introduces higher attenuation and as the distance increases, the  
 352 path loss variations as the function of frequency become more  
 353 pronounced. Finally, the ceramic mug introduces the high-  
 354 est attenuation and the path loss variations as the function  
 355 of frequency become dominant. We can observe that ceramic  
 356 material introduces similar attenuation as a glass at lower fre-  
 357 quencies, i.e., 110–130 GHz, but then the loss increases to over  
 358 100 dB in the range of 140–160 GHz. We can also observe

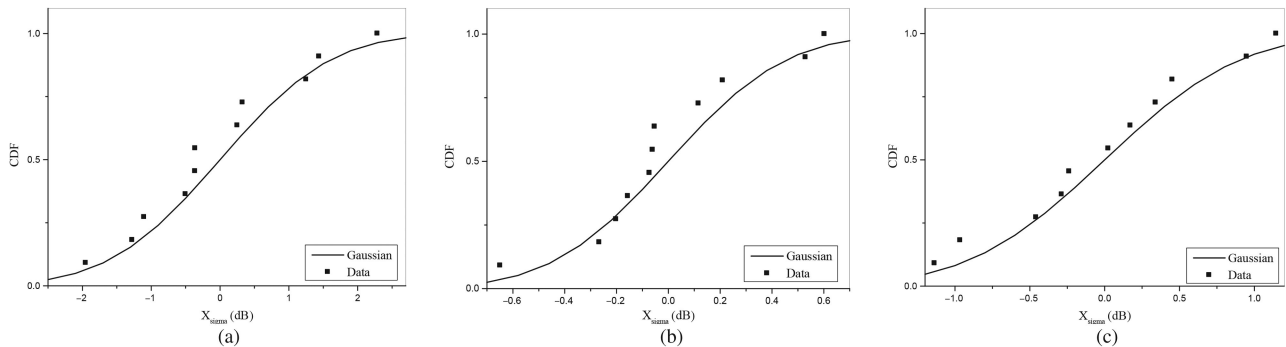
T3:1 TABLE III  
 T3:2 LOG-DISTANCE PATH LOSS MODEL PARAMETERS

	OLOS		
	Glass beaker	Plastic cup	Ceramic mug
Path loss exponent, $\gamma$	2.9519	1.8964	2.1356
Std. deviation, $\sigma$ (dB)	1.3418	0.3757	1.3746
Path loss at $d_0=1\text{m}$ , $PL_0$ (dB)	84.88	77.32	87.94

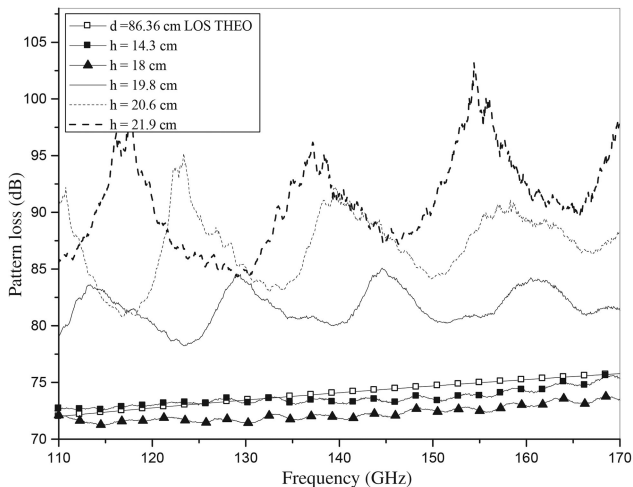
that the maximum of the path loss changes with the separation  
 between the  $T_x$  and  $R_x$ .

Fig. 9(d)–(f) shows the scatter plot of the path loss as a func-  
 tion of T-R separation for glass, plastic, and ceramic OLoS  
 environments, respectively. All 11 distances are used for the  
 scatter plot to obtain the best linear regression fit. As in the  
 LoS case, there are minimal discrepancies among ten consecu-  
 tive measurements because the channel is quasi-static with no  
 moving objects in the environment.

To estimate the path-loss model parameters  $\gamma$  and  $\sigma$  (dB)  
 in (3), we have performed the least-squares linear regression  
 fitting through the scatter of measured path loss points and  
 the results are shown in Fig. 9(d)–(f) for glass, plastic, and  
 ceramic, respectively. The path loss exponents ( $\gamma$ ), standard  
 deviations ( $\sigma$ ), and the path losses at reference distance, 1 m,  
 ( $PL_0$ ) for all three obstruction materials are summarized in  
 Table III. We can observe that the path loss exponent of plas-  
 tic cup is the closest to the LoS path loss exponent value of  
 1.96, which is not surprising since plastic is very transparent  
 at D-band frequencies. For glass and ceramic, due to the con-  
 siderable blockage of LoS path, the path loss exponents have  
 increased above the free-space value of 2. In OLoS scenarios,  
 shadow fading becomes more dominant because of the presence



F10:1 Fig. 10. Zero-mean Gaussian distributed shadow fading and measured shadow fading for OLoS scenarios. (a) Glass beaker. (b) Plastic cup. (c) Ceramic mug.



F11:1 Fig. 11. Variation in path loss with varying height of the ceramic mug  
F11:2 obstruction.

382 of obstructions. To confirm that shadowing can be modeled  
383 as a zero-mean Gaussian distributed random variable, we have  
384 compared the measured distribution of shadow fading with the  
385 Gaussian distribution in Fig. 10. Table III shows that standard  
386 deviation around the mean path loss is the smallest with plastic  
387 obstruction and similar (but much higher) for glass and ceramic  
388 obstructions.

389 Fig. 11 shows variation in OLoS path loss with varying  
390 height of the obstruction, while the T-R separation is fixed at  
391 86.36 cm. As described in Section II-C, the LoS is 20.6 cm  
392 above the table, while  $h$  is varied from 14.3 to 21.9 cm. In  
393 Fig. 11, we can see that the path loss closely follows the  
394 theoretical free-space path loss curve when the LoS path is  
395 clear of obstruction, which corresponds to  $h = 14.3$  cm in the  
396 figure. One interesting observation here is that the path loss  
397 curve for  $h = 18$  cm is about 2 dB below the free-space curve.  
398 Geometrical optics simulations reveal that the ceramic mug  
399 height of 18 cm at separation distance of 86.36 cm places the  
400 top rim of the mug on the boundary of the beam. This results  
401 in the second ray that reflects off the mug's top edge, which  
402 combines vectorially with the first LoS path, leading to a slight  
403 gain in the received power, and therefore slightly lower path  
404 loss than predicted by (1). On the other hand, as  $h$  increases, or  
405 as the mug obstructs more of the LoS path, it is observed that  
406 the path loss increases and becomes more frequency-dependent

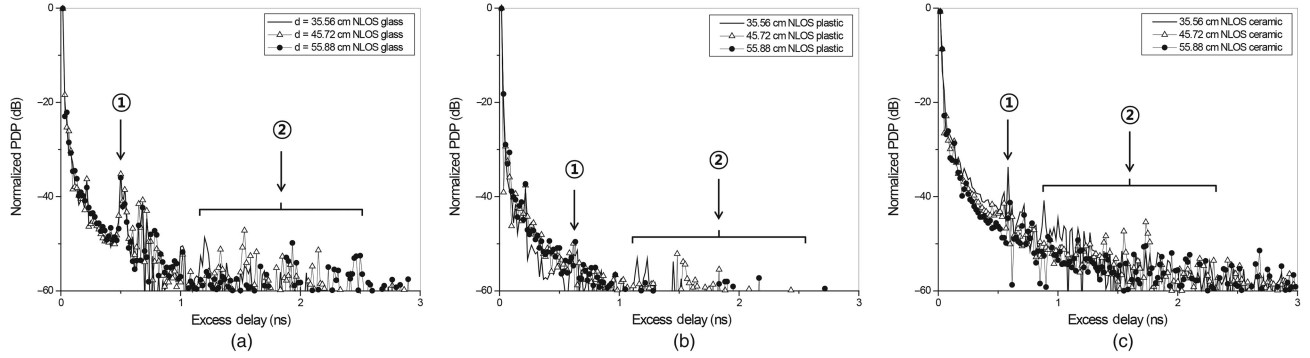
with higher peaks. For this case, our experimental results and  
407 application of uniform geometrical theory of diffraction (UTD)  
408 have revealed the presence of diffraction at the convex surface of the  
409 cylindrical obstruction. The creeping waves or the surface-diffracted  
410 rays that travel around the cylinder in clockwise and counter-clock-  
411 wise directions and their interference seem to be causing the variation  
412 in the measured  $S_{21}$ . Further characterization of this particular  
413 OLoS channel is one of our main future works.  
414  
415

### B. OLoS Multipath Characterization

416  
417 Fig. 12 plots the PDPs for three obstructions: glass, plastic,  
418 and ceramics, respectively. We can observe that all three  
419 PDPs have two distinct segments: one where the reflection peak  
420 appears at the same time delay regardless of the T-R separation  
421 distance (shown as 1 in the figures), followed by the reflection  
422 peaks whose positions depend on the T-R separation distance  
423 (shown as 2 in the figures). Here, we note that the difference  
424 between the first and the second arriving path is always equal  
425 to twice the cup diameter, regardless of the T-R separation  
426 distance, which explains why the multipath marked as 1 appears  
427 at the same excess delay for all distances. Furthermore, from the  
428 excess delay that corresponds to the first multipath (marked as 1  
429 in the figures), we can conclude that this multipath corresponds  
430 to a ray that penetrated the cup, reflected off the wall closer to  
431 the  $R_x$ , reflected off the wall closer to the  $T_x$ , and traveled out-  
432 side the cup to the  $R_x$ . Although the higher order of reflections  
433 might be present, the  $R_x$  sensitivity is not high enough to detect  
434 them.

435 From Fig. 12, we can observe that the PDP for the plastic cup  
436 has weaker reflected paths compared to the glass and ceramic  
437 mugs because most of the energy goes through the plastics and  
438 does not stay trapped inside the obstruction. Furthermore, we  
439 can observe that the PDP for the ceramic mug has significant  
440 reflections only at the distance of 35.56 cm, whereas for 45.72  
441 and 55.88 cm, it is difficult to identify them because the reflec-  
442 tions are significantly attenuated due to material properties.

443 In the PDP section marked as 2 in Fig. 12(a)–(c), we can  
444 observe that the position of the multipath peak depends on the  
445 T-R separation. From the excess delay that corresponds to the  
446 second multipath, we can deduce that the signal has traveled  
447 through the obstruction, was reflected from the  $R_x$  probe head,  
448 was reflected once more off the obstruction, and then received



F12:1 Fig. 12. PDPs for OLoS scenarios. (a) Glass beaker. (b) Plastic cup. (c) Ceramic mug.

T4:1  
T4:2  
T4:3

TABLE IV  
MEAN EXCESS DELAY, RMS DELAY SPREAD, AND COHERENCE  
BANDWIDTH FOR DIFFERENT OBSTRUCTION MATERIALS

d (cm)	Glass beaker			Plastic cup			Ceramic mug		
	$\tau_m$ (ps)	$\tau_{rms}$ (ps)	$B_c$ (GHz)	$\tau_m$ (ps)	$\tau_{rms}$ (ps)	$B_c$ (GHz)	$\tau_m$ (ps)	$\tau_{rms}$ (ps)	$B_c$ (GHz)
35.56	18.06	31.90	4.99	17.03	14.52	10.96	22.21	76.60	2.08
55.88	18.31	45.63	3.49	17.42	23.90	6.66	21.48	62.93	2.53
76.2	18.72	57.19	2.78	16.79	10.85	14.68	20.42	54.98	2.89

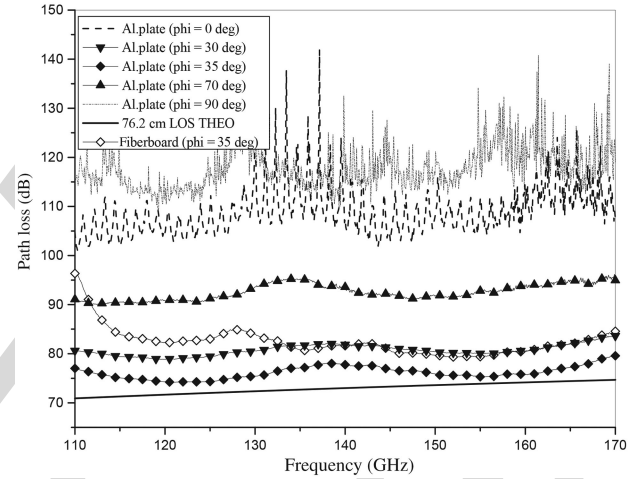
449 by the  $R_x$  antenna. Alternatively, the signal was reflected off  
450 obstruction, then reflected back from the  $T_x$  probe head, and  
451 then traveled through obstruction to the  $R_x$ .

452 Note that the width of the main peak (first arriving path) is the  
453 widest for ceramic mug, which is followed by glass beaker and  
454 plastic cup, as observed in Fig. 12. This indicates that the ratio  
455 of the power associated with the strongest first arriving path to  
456 that of the following reflected paths is the highest for plastic,  
457 while the ratio is the lowest for ceramic. This agrees with the  
458 fact that glass is the most transparent to the waves, allowing  
459 most of the transmitted rays to pass through without multiple  
460 reflections. For ceramics, on the other hand, the transparency of  
461 the material is much lower than glass, which gives rise to more  
462 reflected paths that arrive with delays that are very close to each  
463 other. This high temporal proximity is manifested as clustering  
464 of the reflected paths, which leads to pulse broadening as shown  
465 in Fig. 12(c).

466 The multipath characterization parameters,  $\tau_m$ ,  $\tau_{rms}$ , and  $B_c$ ,  
467 in the OLoS environment with the three different obstructions  
468 for the three T-R spacings, 35.56, 55.88, and 76.2 cm, are  
469 summarized in Table IV. The OLoS channel obstructed by  
470 the plastic cup has the largest coherence bandwidth of almost  
471 11 GHz at 35.56 cm, which is comparable with that of LoS  
472 environment for the same distance. Meanwhile, much narrower  
473 coherence bandwidths below 5 GHz are observed for glass and  
474 ceramic mug obstructions.

#### 475 V. CHARACTERIZATION OF D-BAND RNLOS CHANNEL

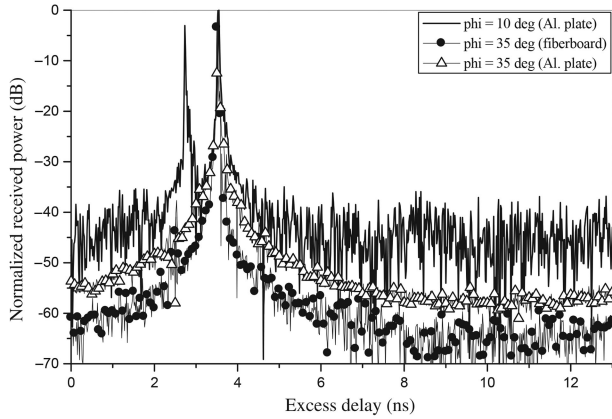
476 Another possible way of communication is through RNLoS  
477 paths. Since the effectiveness of communication will depend  
478 on the reflectivity of the material; here, we compare two dif-  
479 ferent reflectors: aluminum plate and fiberboard. Furthermore,  
480 we investigate the effect of angular orientation of the  $R_x$  on the



F13:1 Fig. 13. Measured RNLoS path loss for different  $R_x$  angles with aluminum  
F13:2 plate, measured RNLoS path loss with fiberboard, and the theoretical free-space  
F13:3 path loss for  $d = 76.2$  cm.

481 received power levels. The  $T_x$  is fixed at  $\phi_T = 35^\circ$ , and the  $R_x$   
482 is rotated between  $\phi_R = 0^\circ$  and  $\phi_R = 90^\circ$ . The angles are mea-  
483 sured from the direct LoS path. The T-R separation distance  
484 has been fixed at  $d = 76.2$  cm. The measured and theoretical  
485 (free-space) path loss for several angles  $\phi_R$  with aluminum  
486 plate and fiberboard as reflectors are shown in Fig. 13. It is  
487 evident from the figure that the level of received power is close-  
488 st to the theoretical LoS level when  $\phi_R = \phi_T = 35^\circ$ , since  
489 the condition  $\phi_R = \phi_T$  ensures that the maximum power is  
490 transferred through specular reflection. The slight discrepancy  
491 from the LoS level can be attributed to the reflection coeffi-  
492 cient of the aluminum plate. As the  $R_x$  angle  $\phi_R$ , deviates from  
493  $35^\circ$ , it is observed that reception becomes weaker and the path  
494 loss significantly increases. At the two extremes,  $\phi = 0^\circ$  and  
495  $\phi = 90^\circ$ , we can observe that the communication is essentially  
496 lost. Furthermore, we can observe that the path loss is higher  
497 when the fiberboard is used as the reflector. This is not surpris-  
498 ing result because the fiberboard has lower reflectivity and  
499 higher surface roughness.

500 The PDPs for RNLoS channel with aluminum plate and  
501 fiberboard as the reflector for the angular positions,  $\phi_R = 10^\circ$   
502 and  $35^\circ$  are presented in Fig. 14. The peaks that coincide at  
503  $\tau = 3.6$  ns represent the paths bouncing off the reflector, while  
504 an additional peak at  $\tau = 2.7$  ns observed for  $\phi_R = 10^\circ$  is a



F14:1 Fig. 14. PDP for different  $R_x$  angles with aluminum plate and fiberboard as  
 F14:2 the reflecting surfaces.

T5:1 TABLE V  
 T5:2 MEAN EXCESS DELAY, RMS DELAY SPREAD, AND COHERENCE  
 T5:3 BANDWIDTH FOR DIFFERENT  $R_x$  ANGULAR POSITIONS

$\Phi_R$ ( $^\circ$ )	Aluminum plate			Cardboard		
	$\tau_m$ (ps)	$\tau_{rms}$ (ps)	$B_c$ (GHz)	$\tau_m$ (ps)	$\tau_{rms}$ (ps)	$B_c$ (GHz)
0	65.72	312.89	0.51	—	—	—
10	89.14	311.20	0.51	—	—	—
35	17.07	9.36	17.00	18.18	36.84	4.32
60	17.17	26.97	5.90	—	—	—
90	132.36	678.48	0.23	—	—	—

505 result of the direct LoS path that arrives before the reflected  
 506 path. Note that for the same  $R_x$  angle of  $\phi_R = 35^\circ$ , alu-  
 507 minium plate and fiberboard produce similar PDPs with a single  
 508 reflected path and no higher order reflections due to the high  
 509 directivity of the antenna.

510 Table V presents the mean excess delay, rms delay spread,  
 511 and coherence bandwidth for several  $R_x$  angular positions in  
 512 RNLoS environment. As expected, we can observe the largest  
 513 coherence bandwidth for  $\phi_R = 35^\circ$ , at which maximum power  
 514 transfer occurs. At the same angle, when the reflecting surface  
 515 is fiberboard, the coherence bandwidth is four times smaller. It  
 516 is also observed that the coherence bandwidth reduces rapidly  
 517 as the  $R_x$  angle deviates from  $35^\circ$ , dropping to megahertz range  
 518 at  $\phi_R = 90^\circ$ .

## 519 VI. CONCLUSION

520 This paper presents measurements and characterization of  
 521 D-band indoor channels. The measurements are performed in  
 522 LoS, OLoS, and RNLoS environments. For OLoS scenario,  
 523 cylindrical objects of different materials are used as obstruc-  
 524 tions. For RNLoS, different surfaces are used as reflectors.  
 525 From the large set of LoS and OLoS measured data, the param-  
 526 eters for single-slope path loss model with shadowing are  
 527 devised. Furthermore, the analysis of multipath propagation is  
 528 performed. The rms delay spread, the mean excess delay, and  
 529 the coherence bandwidth for LoS, OLoS, and RNLoS environ-  
 530 nments are calculated. In addition, the PDPs for LoS, OLoS,  
 531 and RNLoS environments are analyzed. The results show that  
 532 strong multiple reflections from the  $T_x$  and  $R_x$  electronics are

present both in LoS and OLoS environments. Additionally, the  
 results show that glass and ceramic objects in the propaga-  
 tion path produce surface-diffracted rays which clock-wise and  
 counter-clock-wise superposition leads to frequency-dependent  
 path loss. Finally, the results show that the RNLoS measured  
 path loss with aluminum plate as a reflector is very similar to  
 free-space path loss when the angle of incidence and the angle  
 of reflection are equal.

## REFERENCES

- [1] S. Chery, "Edholm's law of bandwidth," *IEEE Spectrum*, vol. 41, no. 7, pp. 58–60, Jul. 2004.
- [2] P. Smulders, "Exploiting the 60 GHz band for local wireless multimedia access: Prospects and future directions," *IEEE Commun. Mag.*, vol. 40, no. 1, pp. 140–147, Aug. 2002.
- [3] M. Fryziel, C. Loyez, L. Clavier, N. Rolland, and P. A. Rolland, "Path-loss model of the 60-GHz indoor radio channel," *Microw. Opt. Technol. Lett.*, vol. 34, no. 3, pp. 158–162, 2002.
- [4] H. Xu, V. Kukshya, and T. S. Rappaport, "Spatial and temporal characteristics of 60-GHz indoor channels," *IEEE J. Sel. Areas Commun.*, vol. 20, no. 3, pp. 620–630, Apr. 2002.
- [5] N. Moraitis and P. Constantinou, "Indoor channel measurements and characterization at 60 GHz for wireless local area network applications," *IEEE Trans. Antennas Propag.*, vol. 52, no. 12, pp. 3180–3189, Dec. 2004.
- [6] T. Zwick, T. J. Beukema, and H. Nam, "Wideband channel sounder with measurements and model for the 60 GHz indoor radio channel," *IEEE Trans. Veh. Technol.*, vol. 54, no. 4, pp. 1266–1276, Jul. 2005.
- [7] H. Yang, P. F. M. Smulders, and M. H. A. J. Herben, "Indoor channel measurements and analysis in the frequency bands 2 GHz and 60 GHz," in *Proc. IEEE Symp. Pers. Indoor Mob. Radio Commun.*, Sep. 2005, pp. 1–5.
- [8] S. Geng, J. Kivinen, X. Zhao, and P. Vainikainen, "Millimeter-wave propagation channel characterization for short-range wireless communications," *IEEE Trans. Veh. Technol.*, vol. 58, no. 1, pp. 3–13, Jan. 2009.
- [9] M. Peter and W. Keusgen, "Analysis and comparison of indoor wideband radio channels at 5 and 60 GHz," in *Proc. Eur. Conf. Antennas Propag. (EUCAP'09)*, Mar. 2009, pp. 3830–3834.
- [10] T. S. Rappaport *et al.*, "Millimeter wave mobile communications for 5G cellular: It will work!" *IEEE Access*, vol. 1, pp. 335–349, May 2013.
- [11] P. H. Siegel, "Terahertz technology," *IEEE Trans. Microw. Theory Techn.*, vol. 50, no. 3, pp. 910–928, Mar. 2002.
- [12] T. Kleine-Ostmann, K. Pierz, G. Hein, P. Dawson, and M. Koch, "Audio signal transmission over THz communication channel using semiconductor modulator," *Electron. Lett.*, vol. 40, pp. 124–126, Jan. 2004.
- [13] C. Jastrow *et al.*, "300 GHz transmission system," *Electron. Lett.*, vol. 44, pp. 213–215, Jan. 2008.
- [14] C. Jastrow *et al.*, "Wireless digital data transmission at 300 GHz," *Electron. Lett.*, vol. 46, pp. 661–687, Apr. 2010.
- [15] S. Priebe *et al.*, "Channel and propagation measurements at 300 GHz," *IEEE Trans. Antennas Propag.*, vol. 59, no. 5, pp. 1688–1698, May 2011.
- [16] R. Piesiewicz *et al.*, "Short-range ultra-broadband terahertz communications: Concepts and perspectives," *IEEE Antennas Propag. Mag.*, vol. 49, no. 6, pp. 24–39, Jun. 2007.
- [17] R. Piesiewicz *et al.*, "Scattering analysis for the modeling of THz communication systems," *IEEE Trans. Antennas Propag.*, vol. 55, no. 11, pp. 3002–3009, Nov. 2007.
- [18] Y. Yang, M. Mandehgar, and D. Grischkowsky, "Broadband THz pulse transmission through the atmosphere," *IEEE Trans. Terahertz Sci. Technol.*, vol. 1, no. 1, pp. 264–273, Sep. 2011.
- [19] J. M. Jornet and I. F. Akyildiz, "Channel modeling and capacity analysis for electromagnetic wireless nanonetworks in the terahertz band," *IEEE Transactions on Wireless Communications*, vol. 10, no. 10, pp. 3211–3221, Oct. 2011.
- [20] R. Piesiewicz *et al.*, "Terahertz characterisation of building materials," *IEEE Electron. Lett.*, vol. 41, no. 18, pp. 1002–1004, Sep. 2005.
- [21] C. Jansen, R. Piesiewicz, D. Mittleman, T. Kürner, and M. Koch, "The impact of reflections from stratified building materials on the wave propagation in future indoor terahertz communication systems," *IEEE Trans. Antennas Propag.*, vol. 56, no. 5, pp. 1413–1419, May 2008.

- [22] S. Priebe *et al.*, "A comparison of indoor channel measurements and ray tracing simulations at 300 GHz," in *Proc. Int. Conf. Infrared Millim. Terahertz Waves (IRMMW-THz)*, Sep. 2010.
- [23] M. Jacob *et al.*, "Diffraction in mm and sub-mm wave indoor propagation channels," *IEEE Trans. Microw. Theory Techn.*, vol. 60, no. 3, pp. 833–844, Mar. 2012.
- [24] S. Kim and A. Zajić, "Path loss model for 300-GHz wireless channels," in *Proc. IEEE Int. Symp. Antennas Propag.*, Memphis, Tennessee, USA, Jul. 2014, pp. 1–2.
- [25] S. Kim and A. Zajić, "Statistical characterization of 300-GHz propagation on a desktop," *IEEE Trans. Veh. Technol.*, to be published.
- [26] T. Kosugi *et al.*, "120-GHz Tx/Rx waveguide modules for 10-Gbit/s wireless link system," in *Proc. IEEE CSICS Dig.*, Oct. 2006, pp. 25–28.
- [27] I. Sarkas, E. Laskin, J. Hasch, P. Chevalier, and S. P. Voinigescu, "Second generation transceivers for D-band radar and data communication applications," in *Proc. IEEE IMS Dig.*, May 2010, pp. 1328–1331.
- [28] E. Laskin *et al.*, "Nanoscale CMOS transceiver design in the 90–170 GHz range," *IEEE Trans. Microw. Theory Techn.*, vol. 57, no. 12, pp. 3477–3490, Dec. 2009.
- [29] G. Liu and E. K. Seo, "Detecting snowfall over land by satellite high-frequency microwave observations: The lack of scattering signature and a statistical approach," *J. Geophys. Res.: Atmos.*, vol. 118, pp. 1376–1387, Feb. 2013.
- [30] Z. Chen and J. C. Cao, "Channel characterization at 120 GHz for future indoor communication systems," *Chin. Phys. B*, vol. 22, no. 5, p. 059201, 2013.
- [31] A. Zajić, *Mobile-to-Mobile Wireless Channels*. Norwood, MA, USA: Artech House, Jan. 2013.



**Seunghwan Kim** (S'14) was born in Seoul, South Korea, in 1986. He received the Bachelor of Applied Science degree in electrical engineering from the University of Waterloo, Waterloo, ON, Canada, in 2009. He is currently pursuing the Ph.D. degree in electrical engineering at Georgia Institute of Technology, Atlanta, GA, USA.

During his degree, he worked as a Research Assistant with the Telecommunication Group, Korea Electrotechnology Research Institute (KERI), Changwon, Korea, and as a Hardware Engineer with

Mitel Networks, Kanata, ON, Canada.



**Wasif Tanveer Khan** (S'10–M'15) received the B.Sc. degree in electrical engineering from the University of Engineering and Technology, Lahore, Pakistan, in 2005, and the M.S. and Ph.D. degrees in electrical and computer engineering from Georgia Institute of Technology, Atlanta, GA, USA, in 2010 and 2014, respectively.

From January 2006 to December 2008, he was a Lecturer with the National University of Computer and Emerging Sciences-FAST, Lahore, Pakistan. Since January 2015, he has been working as an Assistant Professor with the Department of Electrical Engineering, Lahore University of Management Sciences, Lahore, Pakistan. He has authored/coauthored more than 35 research papers in peer-reviewed conferences and journals. His research interests include the RF and microwave system design, millimeter wave circuit and package design, multilayer organic packaging, on-chip and off-chip antenna design, and phased array systems.

Dr. Khan has been the publications Chair for four IEEE conferences: RWS, PAWR, WisNet, and BioWireless, since 2010. Since 2011, he has also been a Technical Program Committee (TPC) member for IEEE Radio and Wireless Symposium (RWS). He was the recipient of a MS leading to Ph.D. fullbright Scholarship.



**Alenka Zajić** (S'99–M'09–SM'13) received the B.Sc. and M.Sc. degrees in electrical engineering from the University of Belgrade, Belgrade, Serbia, in 2001 and 2003, respectively, and the Ph.D. degree in electrical and computer engineering from Georgia Institute of Technology, Atlanta, GA, USA, in 2008.

Currently, she is an Assistant Professor with the School of Electrical and Computer Engineering, Georgia Institute of Technology. Prior to that, she was a Visiting Faculty at the School of Computer Science, Georgia Institute of Technology, a Postdoctoral Fellow with the Naval Research Laboratory, and Design Engineer with Skyworks Solutions Inc. Her research interests include electromagnetics, wireless communications, signal processing, and computer engineering.

Dr. Zajić was the recipient of the Neal Shepherd Memorial Best Propagation Paper Award, the Best Paper Award at ICT 2008, the Best Student Paper Award at WCNC 2007, the Dan Noble Fellowship in 2004, awarded by Motorola Inc., and the IEEE VEHICULAR TECHNOLOGY SOCIETY for quality impact in the area of vehicular technology. Currently, she is an Editor for IEEE TRANSACTIONS ON WIRELESS COMMUNICATIONS and the Chair of the IEEE MTT/AP Atlanta Chapter.



**John Papapolymerou** (F'xx) received the B.S.E.E. degree from the National Technical University of Athens, Athens, Greece, in 1993, and the M.S.E.E. and Ph.D. degrees from the University of Michigan, Ann Arbor, MI, USA, in 1994 and 1999, respectively.

From 1999 to 2001, he was an Assistant Professor with the Department of Electrical and Computer Engineering, University of Arizona, Tucson, AZ, USA, and during 2000 and 2003, he was a Visiting Professor at the University of Limoges, Limoges, France. From 2001 to 2005 and 2005 to 2009, he was an Assistant Professor and Associate Professor, respectively, with the School of Electrical and Computer Engineering, Georgia Institute of Technology, Atlanta, GA, USA, where he is currently the Ken Byers Professor. He has authored or coauthored over 350 publications in peer-reviewed journals and conferences. His research interests include the implementation of micromachining techniques and MEMS devices in microwave, millimeter-wave and THz circuits and the development of both passive and active planar circuits and antennas on semiconductor (Si/SiGe, GaAs) and organic substrates (liquid crystal polymer-LCP, LTCC) for system-on-a-chip (SOC)/ system-on-a-package (SOP) RF front ends.

Dr. Papapolymerou currently serves as Editor-in-Chief for IEEE MICROWAVE AND WIRELESS COMPONENTS LETTERS (MWCL). He has also served as an Associate Editor for IEEE TRANSACTIONS ON MICROWAVE THEORY AND TECHNIQUES from 2010 to 2012, and as Chair for Commission D of the US National Committee of URSI from 2009 to 2011. He was also an Associate Editor for IEEE MWCL (2004–2007), and IEEE TRANSACTIONS ON ANTENNAS AND PROPAGATION (2004–2010). During 2004, he was the Chair of the IEEE MTT/AP Atlanta Chapter. He was the recipient of the 2012 IEEE ANTENNAS AND PROPAGATION SOCIETY (AP-S) H.A. Wheeler Prize Paper Award, the 2010 IEEE AP-S John Kraus Antenna Award, the 2009 IEEE MICROWAVE THEORY AND TECHNIQUES-SOCIETY (MTT-S) Outstanding Young Engineer Award, the 2009 School of ECE Outstanding Junior Faculty Award, the 2004 Army Research Office (ARO) Young Investigator Award, the 2002 National Science Foundation (NSF) CAREER award, the Best Paper Award at the 3rd IEEE International Conference on Microwave and Millimeter-Wave Technology (ICMMT2002), Beijing, China, and the 1997 Outstanding Graduate Student Instructional Assistant Award presented by the American Society for Engineering Education (ASEE), the University of Michigan Chapter.

## QUERIES

- Q1: Please provide issue number for Ref. [10].
- Q2: Please provide page range for Ref. [22].
- Q3: Please update Ref. [25].
- Q4: Please provide field of studies for “B.S.E.E., M.S.E.E., and Ph.D.” degrees and membership history (year) of author “John Papapolymerou.”

IEEE  
Proof